SIAM J. IMAGING SCIENCES
Vol. 11, No. 2, pp. 1680–1716

Imaging Extended Reflectors in a Terminating Waveguide*

Chrysoula Tsogka†, Dimitrios A. Mitsoudis‡, and Symeon Papadimitropoulos§

Abstract. We consider the problem of imaging extended reflectors in terminating waveguides. We form the image by back-propagating the array response matrix projected on the waveguide's nonevanescent modes. The projection is adequately defined for any array aperture size covering fully or partially the waveguide's vertical cross-section. We perform a resolution analysis of the imaging method and show that the resolution is determined by the central frequency, while the image's signal-to-noise ratio improves as the bandwidth increases. The robustness of the imaging method is assessed with fully nonlinear scattering data in terminating waveguides with complex geometries.

Key words. array imaging, terminating waveguides, partial aperture

AMS subject classifications. 35R30, 74J20, 74J25

DOI. 10.1137/17M1159051

1. Introduction.

In this paper we consider the problem of imaging extended reflectors in terminating acoustic waveguides with complex geometries, such as the one depicted in Figure 1 (see section 2). Specifically, we assume that the waveguide $\Omega \subset \mathbb{R}^2$ consists of a semi-infinite strip $\Omega_{L^-} = (-\infty, L) \times (0, D)$ in which the speed of propagation may depend only on the cross-range variable x, i.e., $c = c(x)$, and a bounded domain Ω_{L^+} in which the speed of propagation may be fully inhomogeneous, i.e., $c = c(z, x)$, and contains the reflector that we wish to image. Although we restrict our presentation to the two-dimensional case, the proposed imaging methodology can be extended in a straightforward manner to a three-dimensional waveguide with bounded cross-section. We illustrate this with some numerical results in the three-dimensional case.

Our data is the array response matrix for the scattered field collected on an array of transducers which can play the dual role of emitters and receivers. This is a three-dimensional data structure $[\widehat{\Pi}]_{srl}$ that depends on the location of the source $\vec{\boldsymbol{x}}_s$, $s = 1, \ldots, N_s$, the receiver $\vec{\boldsymbol{x}}_r$, $r = 1, \ldots, N_r$, and the frequency ω_l, $l = 1, \ldots, N_f$. The element $\widehat{\Pi}(\vec{\boldsymbol{x}}_s, \vec{\boldsymbol{x}}_r; \omega_l)$ denotes the response recorded at $\vec{\boldsymbol{x}}_r$ when a unit amplitude signal at frequency ω_l is sent from a

*Received by the editors November 29, 2017; accepted for publication (in revised form) April 5, 2018; published electronically June 28, 2018.
http://www.siam.org/journals/siims/11-2/M115905.html
Funding: Part of this material is based on work supported by the National Science Foundation under grant DMS-1439786 while the authors were in residence at the Institute for Computational and Experimental Research in Mathematics (ICERM) in Providence, RI during the fall 2017 semester. The first author was also partially supported by AFOSR FA9550-17-1-0238. The second and third authors were also supported by IACM/FORTH during their participation in ICERM's semester program.
†Applied Math Unit, University of California, Merced, Merced, CA 95343 (ctsogka@ucmerced.edu).
‡Department of Energy Technology Engineering, Technological Educational Institute of Athens, Ag. Spiridona 17, 12210 Egaleo, Greece, and IACM/FORTH, Heraklion 70013, Crete, Greece (dmits@teiath.gr).
§Department of Mathematics & Applied Mathematics, University of Crete & IACM/FORTH, Heraklion 70013, Crete, Greece (spapadem@tem.uoc.gr).

point source at $\vec{\boldsymbol{x}}_s$. Furthermore, we consider that the array is located in Ω_{L^-}, has an equal number of sources and receivers $N_s = N_r = N$, and may span fully or partially the vertical cross-section of the waveguide.

Imaging in waveguides is of particular interest in underwater acoustics [9, 19, 32, 17, 25, 29, 13, 7], where one wants to characterize sound speed inhomogeneities in shallow ocean environments, with applications in sonar, marine ecology, seabed imaging, etc. Moreover, imaging in waveguides is also applicable in inspections of underground pipes using acoustic waves [23, 28] and in nondestructive evaluation of materials where elastic wave propagation should be considered [6]. In any case, this is a challenging inverse scattering problem since in a waveguide geometry the wave field may be decomposed in a finite number of propagating modes and an infinite number of evanescent modes. The evanescent part of the wave field is in general not available in the measured data because it decays exponentially fast with the propagation distance. Our assumptions about Ω_{L^-} allow us to apply the technique of separation of variables, so we let $\{X_n\}_{n=1}^{\infty}$ denote the orthonormal eigenfunctions of the associated Sturm–Liouville eigenvalue problem in a vertical cross-section of Ω_{L^-} and let M be the number of propagating modes.

In this paper we propose and analyze an imaging method that relies only on the propagating modes in the waveguide. The idea of formulating the inverse scattering problem in terms of the propagating modes has been considered by several authors; indicatively we refer to the relatively recent works [13, 27, 7]. In [13] the problem of reconstructing weak inhomogeneities located in an infinite strip is addressed, and the solution of the linearized inverse scattering problem is obtained using the spectral decomposition of the far-field matrix. We note that in this case the measurements consist of both the transmitted and the reflected (backscattered) field. In [27] the problem of selective focusing on small scatterers in two-dimensional acoustic waveguides is considered, and the spectral decomposition of the time-reversal operator is analyzed in this setting. In [7] the authors establish a modal formulation for the linear sampling method (LSM) [12] for imaging extended reflectors in waveguides. The extension to the case of anisotropic scatterers that may touch the waveguide boundaries is carried out in [23], where both the LSM and the reciprocity gap method (RGM) [11] are studied theoretically and numerically. The case of imaging cracks in acoustic waveguides is considered in [8] using LSM and the factorization method [21]. In all the aforementioned works the waveguide geometry is infinite in one dimension.

The case of a semi-finite, terminating waveguide such as the one considered here was first studied to the best of our knowledge in [4] for electromagnetic waves in three dimensions. In particular in [4] the forward data model was derived using Maxwell's equations, and two imaging methods were formulated: (a) reverse time migration (phase conjugation in the frequency domain) obtained by applying the adjoint of the forward operator to the data, and (b) an l_1-sparsity promoting optimization method.

Our imaging approach is also inspired by phase conjugation and consists of back-propagating the array response matrix projected on the M waveguide's propagating modes. It is important to note that the projection on the propagating modes is not an obvious procedure when the array does not span the whole aperture of the waveguide. Following our previous work [31] we define this modal projection adequately using the eigenvalue decomposition of the matrix $A_{\text{arr}} \in \mathbb{R}^{M\times M}$, whose mnth component is the integral over the array aperture of

the product $X_n(\cdot)X_m(\cdot)$. The orthonormality of X_n implies that A_{arr} reduces to the identity matrix when the array spans the entire vertical cross-section of the waveguide. The properties of the eigenvalues and eigenvectors of A_{arr} were analyzed in detail in [31] for the partial aperture case. We show in particular that there is no loss of information and therefore no change in the image as long as the minimal eigenvalue of A_{arr} remains above a threshold value ϵ, which depends on the noise level in the data or equals the machine precision in the noiseless case. As the array aperture decreases, the number of the eigenvalues that fall below ϵ increases, and consequently the quality of the image deteriorates (see [31]).

To analyze the resolution of the proposed imaging method, we consider the case of a point reflector and prove that the single frequency point spread function equals the square of the imaginary part of the Green's function. This is established using the Kirchhoff–Helmholtz identity, which we derive for the terminating waveguide configuration. Furthermore, for the simple geometry of a semi-infinite strip in two dimensions, a detailed resolution analysis is carried out. This determines the resolution of the imaging method, which depends only on the central frequency and equals half the wavelength in both directions. Although the bandwidth does not affect the resolution, it does play an important role as it significantly improves the signal-to-noise ratio of the image. This is shown theoretically and is also confirmed by our numerical simulations.

Imaging in the terminating waveguide geometry allows for improvement in the reconstructions compared to the infinite waveguide case. This is because multiple-scattering reflections that bounce off the terminating boundary of the waveguide provide multiple views of the reflector that are not available in the infinite waveguide case. To benefit from this multipathing, we need to know or determine the boundary of the waveguide prior to imaging the reflector. In this work we consider that the waveguide boundary is known. We refer the reader to [3] for a study of source imaging in waveguides with random boundary perturbations, where it is shown that uncertainty in the location of the boundaries can be mitigated using filters that imply a somewhat reduced resolution. Moreover, it is shown in [3] that there is an optimal trade-off between robustness and resolution which can be adaptively determined during the image formation process.

The robustness of the proposed imaging method is assessed with fully nonlinear scattering data obtained using the Montjoie software [24]. The use of this software allows us to model wave propagation in waveguides with complicated geometries and study the reconstruction of diverse reflectors. For all the examples considered, we have obtained significant improvement in the reconstruction in the terminating waveguide geometry as compared to the infinite case. We have also studied the robustness of the method for different array apertures ranging from full to one-fourth of the waveguide's vertical cross-section, and we assess its performance under the effect of measurement noise. The quality of the image deteriorates as we decrease the array aperture, but our imaging results remain very satisfactory even with an array aperture equal to one-fourth of the full one. In most of the examples, we consider that the multistatic array response matrix is available. However, the same method can also be applied to synthetic array data obtained with a single transmit/receive element. We obtain good reconstructions for this reduced data modality but for larger array apertures that cover at least half of the waveguide's width in the vertical direction.

The paper is organized as follows. In section 2 we present the formulation of the problem.

In section 3 we describe our imaging methodology inspired by phase conjugation for both the passive imaging configuration, which concerns imaging a source, and the active setup, which refers to imaging a reflector. The resolution analysis is carried out in section 4 for single and multiple frequency imaging. Finally, in section 5 we illustrate the performance of our approach with numerical simulations in two and three dimensions.

2. Formulation of the problem. In this work, we study the problem of imaging extended reflectors in a two-dimensional terminating waveguide, as shown in Figure 1. The reflector is illuminated by an active vertical array $\mathcal{A}$, composed of N transducers that act as sources and receivers. The array may span the whole vertical cross-section of the waveguide or part of it. The array transducers are assumed to be distributed uniformly, and densely enough; that is, the interelement distance h is considered to be small—typically a fraction of the wavelength λ. The term *extended* indicates that the reflectors are comparable in size to λ.

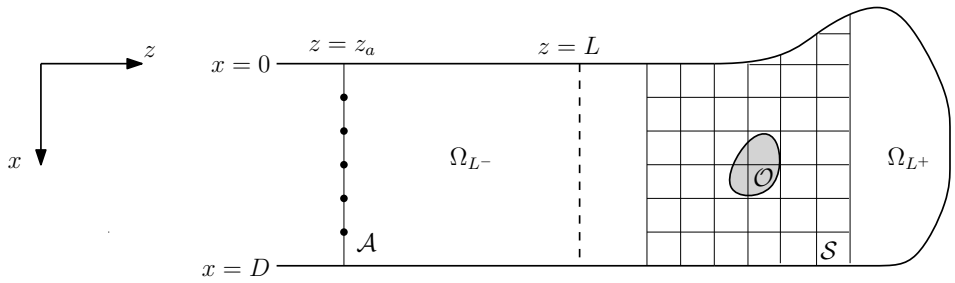

Figure 1. *Schematic representation of the semi-infinite waveguide.*

We also assume that the array measurements can be cast in the form of the so-called array response matrix, denoted by $\widehat{\Pi}$. This is an $N \times N$ complex matrix whose (r, s) entry is the Fourier transform of the time traces of the echoes recorded at the rth receiver when the sth source emits a signal. In particular, we shall use the array response matrix for the scattered field that is due to the presence of an extended reflector $\mathcal{O}$ located somewhere in the bounded part of the waveguide delimited by the cross-section at $z = L$ (see Figure 1). As usual, the scattered field is determined by subtracting the incident field from the total field.

Specifically, we consider a Cartesian coordinate system (z, x), where z denotes the main direction of propagation—called hereafter *range*—and x denotes the cross-range direction taken to be positive downwards. Our terminating waveguide Ω consists of two subdomains: the semi-infinite strip $\Omega_{L^-} = (-\infty, L) \times (0, D)$ and a bounded domain in $\mathbb{R}^2$ denoted by Ω_{L^+}. Let us also assume that all the inhomogeneities of the medium are contained in Ω_{L^+}, while the medium is homogeneous in the semi-infinite strip Ω_{L^-} (i.e., the wave speed may depend on the range and the cross-range in Ω_{L^+}) and varies smoothly to the constant value that the speed has for $z \leq L$. Note that the assumption of a constant wave speed in Ω_{L^-} may be relaxed by requiring the speed to depend on the cross-range variable x. However, to facilitate the presentation in this paper we will consistently assume that Ω_{L^-} is filled with a homogeneous medium.

The total field for our waveguide in the presence of a scatterer solves the scalar wave

equation

$$\Delta p^{\rm tot}(t,\vec{\boldsymbol{x}}) - \frac{1}{c(\vec{\boldsymbol{x}})^2}\frac{\partial^2 p^{\rm tot}(t,\vec{\boldsymbol{x}})}{\partial t^2} = -f(t,\vec{\boldsymbol{x}}), \tag{1}$$

where $\vec{\boldsymbol{x}} = (z,x) \in \Omega$ and the source term $f(t,\vec{\boldsymbol{x}})$ models a point-like source with time-harmonic dependence. Equation (1) is supplemented by homogeneous Dirichlet conditions on the boundary of Ω. The scatterer is modeled as an acoustically hard scatterer with a homogeneous Neumann condition on $\partial\mathcal{O}$, and a suitable outgoing radiation condition is assumed as $z \to -\infty$. Moreover, we assume that the medium is quiet for $t \le 0$, i.e., $p^{\rm tot}(t,\vec{\boldsymbol{x}}) = 0$ for $t \le 0$. Note that the scalar wave equation that we consider here is used quite often instead of the full Maxwell's or elastic wave equations since it captures the main features of the scattering problem.

By applying the Fourier transform

$$\widehat{p}^{\rm tot}(\omega,\vec{\boldsymbol{x}}) = \int \mathrm{e}^{i\omega t} p^{\rm tot}(t,\vec{\boldsymbol{x}})dt \tag{2}$$

on (1), we obtain the Helmholtz equation for the total field

$$-\Delta\widehat{p}^{\rm tot}(\omega,\vec{\boldsymbol{x}}) - k^2\eta(\vec{\boldsymbol{x}})\,\widehat{p}^{\rm tot}(\omega,\vec{\boldsymbol{x}}) = \widehat{f}(\omega,\vec{\boldsymbol{x}}), \quad \vec{\boldsymbol{x}} \in \Omega, \tag{3}$$

where ω is the angular frequency, $k = \omega/c_0$ is the (real) wavenumber, and $\eta(\vec{\boldsymbol{x}}) = c_0^2/c^2(\vec{\boldsymbol{x}})$ is the index of refraction. (Notice that $\eta(\vec{\boldsymbol{x}}) = 1$ for all $\vec{\boldsymbol{x}} \in \Omega_{L^-}$.)

Let also $\widehat{G}(\vec{\boldsymbol{x}},\vec{\boldsymbol{x}}_s;\omega)$ denote the Green's function for the Helmholtz operator (and the associated boundary conditions) due to a point source located at $\vec{\boldsymbol{x}}_s = (z_s,x_s) \in \Omega$ and for a single frequency ω, i.e., $\widehat{G}(\vec{\boldsymbol{x}},\vec{\boldsymbol{x}}_s;\omega)$ is the solution of

$$-\Delta\widehat{G}(\vec{\boldsymbol{x}},\vec{\boldsymbol{x}}_s;\omega) - k^2\eta(\vec{\boldsymbol{x}})\widehat{G}(\vec{\boldsymbol{x}},\vec{\boldsymbol{x}}_s;\omega) = \delta(\vec{\boldsymbol{x}}-\vec{\boldsymbol{x}}_s). \tag{4}$$

Finally, let (μ_n, X_n) be the eigenvalues and corresponding orthonormal eigenfunctions of the following vertical eigenvalue problem in the homogeneous part of the waveguide Ω_{L^-}:

$$X_n''(x) + \mu_n X(x) = 0, \qquad X_n(0) = X_n(D) = 0. \tag{5}$$

Henceforth we shall assume that there exists an index M such that the constant value k^2 of the wavenumber satisfies in Ω_{L^-}:

$$\lambda_M < k^2 < \lambda_{M+1}.$$

In other words, M is the number of *propagating modes* in Ω_L^-. Let us also denote the horizontal wavenumbers in Ω_L^- by

$$\beta_n = \begin{cases} \sqrt{k^2-\mu_n}, & 1 < n < M, \\ \mathrm{i}\sqrt{\mu_n - k^2}, & n > M+1. \end{cases} \tag{6}$$

In what follows we will assume that the problems for the incident and the total fields, which are governed by the Helmholtz equation and satisfy the boundary conditions in the

perturbed semi-infinite cylinder described before, are well-posed. For example, in the case where $\eta(\vec{\boldsymbol{x}}) = 1$ everywhere in Ω, it has been proved in [15] that the problem for the incident field is well-posed under the assumption that $k^2 \notin \Lambda \cup \{\mu_n\}_{n=1}^{\infty}$, where Λ is the point spectrum of the negative Dirichlet Laplacian acting on $L^2(\Omega)$. This set Λ, which may be empty in some cases, is known to be at most countable, with no finite accumulation point; see [20]. For the total field there are examples in infinite waveguides that suggest existence of the so-called trapped modes, i.e., nonzero localized solutions of the associated homogeneous problem; see, e.g., [14].

3. Imaging.

Our main objective in this work is to form images of extended reflectors that lie somewhere in a terminating waveguide like the one described in the previous section. The usual steps that one may follow to this end are to first identify a search domain $\mathcal{S}$ (see Figure 1), discretize it using a grid, and then compute the value of an appropriate imaging functional in each grid point in $\mathcal{S}$. It is expected that these values, when they are graphically displayed in the search domain, will exhibit peaks that indicate the presence of the reflector.

3.1. Imaging with a full aperture array.

We shall first consider the easier case where the array spans the whole vertical cross-section of the waveguide. Moreover, although we are interested in imaging extended reflectors, we will first examine the so-called passive imaging problem in order to motivate the use of the imaging functional that we will introduce next.

3.1.1. Passive imaging.

Let us assume that a point source of unit strength, located at the point $\vec{\boldsymbol{x}}_s = (z_s, x_s) \in \Omega$, emits a signal that is recorded on a vertical array $\mathcal{A}$ located in Ω_{L^-}. Moreover, we assume that the array $\mathcal{A} = \{\vec{\boldsymbol{x}}_r = (z_a, x_r)\}_{r=1}^{N}$ $(z_a < L)$ spans the whole vertical cross-section of the waveguide as illustrated in Figure 2. Our aim is to find the location of the source. In this case the array response matrix $\widehat{\Pi}$ at frequency ω reduces to an $N \times 1$ vector, whose rth component equals the Green's function evaluated at receiver $\vec{\boldsymbol{x}}_r$ due to the source $\vec{\boldsymbol{x}}_s$, i.e.,

$$\widehat{\Pi}(\vec{\boldsymbol{x}}_r; \omega) = \widehat{G}(\vec{\boldsymbol{x}}_r, \vec{\boldsymbol{x}}_s; \omega). \tag{7}$$

In what follows we consider a monochromatic source, and to simplify the notation we suppress parameter ω from the imaging functional and the Green's function. The dependence on ω will be recalled in subsection 4.2 where imaging with multiple frequency data is considered.

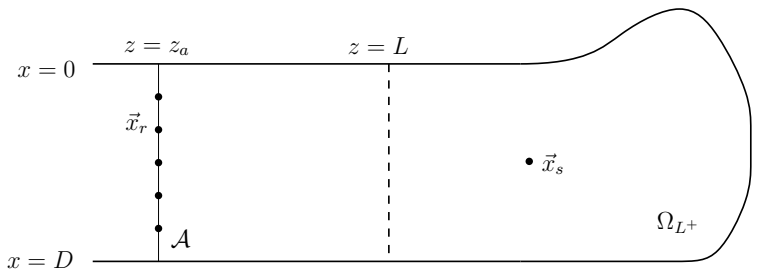

Figure 2. *Passive imaging setup in a terminated waveguide.*

The imaging functional that we propose to use is based on the concept of phase conjugation, which may be physically interpreted by virtue of the Huygen's principle. As pointed out

in [18], the Huygen's principle states that a propagating wave may be viewed as a superposition of wavelets re-emitted from a fictitious surface with amplitudes proportional to those of the original wave. In phase conjugation, which may be seen as the equivalent of time reversal in the frequency domain, the re-emitted wavelets' amplitudes are proportional to the complex conjugate of the corresponding ones in the original wave. These remarks naturally lead one to define the following classical phase conjugation imaging functional:

$$\mathcal{I}^{\rm pc}(\vec{\boldsymbol{y}}^s) = \int_{\mathcal{A}} \overline{\widehat{G}(\vec{\boldsymbol{x}}_r, \vec{\boldsymbol{x}}_s)} \widehat{G}(\vec{\boldsymbol{y}}^s, \vec{\boldsymbol{x}}_r) dx, \tag{8}$$

where $\vec{\boldsymbol{x}}_r = (z_a, x) \in \mathcal{A}$ and $\vec{\boldsymbol{y}}^s \in \mathcal{S}$. However, if we assume for a moment that apart from recording the value of the field on the array we would be able to record its normal derivative as well, then we may define the following imaging functional, which as we will show next has very nice theoretical properties. Thus let

$$\mathcal{I}(\vec{\boldsymbol{y}}^s) := \int_{\mathcal{A}} \left(\overline{\widehat{G}(\vec{\boldsymbol{x}}_r, \vec{\boldsymbol{x}}_s)} \nabla \widehat{G}(\vec{\boldsymbol{x}}_r, \vec{\boldsymbol{y}}^s) - \widehat{G}(\vec{\boldsymbol{x}}_r, \vec{\boldsymbol{y}}^s) \overline{\nabla \widehat{G}(\vec{\boldsymbol{x}}_r, \vec{\boldsymbol{x}}_s)} \right) \cdot \nu \, dx, \tag{9}$$

where ν is the outward-pointing unit normal vector to $\mathcal{A}$. Of course this functional is more complicated than phase conjugation, but the following proposition shows that in order to compute $\mathcal{I}(\vec{\boldsymbol{y}}^s)$ in a terminating waveguide it is required to know only the values of the wave field on the array and not its derivatives. We note that the form of the integral that appears in the right-hand side of (9) is also met in the context of the so-called reciprocity gap method; see, e.g., [11, 23].

Proposition 3.1 (Kirchhoff–Helmholtz identity). *Assume that a point source is located in the terminating waveguide described in section 2 (see also Figure 2) and that a vertical array $\mathcal{A}$, which spans the whole vertical cross-section of the waveguide, is located in Ω_{L^-}. Then, the imaging functional defined in (9) satisfies the following Kirchhoff–Helmholtz identity:*

$$\mathcal{I}(\vec{\boldsymbol{y}}^s) = \widehat{G}(\vec{\boldsymbol{y}}^s, \vec{\boldsymbol{x}}_s) - \overline{\widehat{G}(\vec{\boldsymbol{y}}^s, \vec{\boldsymbol{x}}_s)} = 2i \mathrm{Im}\, \widehat{G}(\vec{\boldsymbol{y}}^{\rm s}, \vec{\boldsymbol{x}}_s). \tag{10}$$

Moreover, we can show that

$$\mathcal{I}(\vec{\boldsymbol{y}}^s) = 2i \sum_{n=1}^{M} \beta_n \, \overline{\widehat{G}_n(z_a, \vec{\boldsymbol{x}}_s)} \, \widehat{G}_n(z_a, \vec{\boldsymbol{y}}^s), \tag{11}$$

where $\widehat{G}_n(z_a, \cdot)$, $n = 1, \ldots, M$, denote the first M Fourier coefficients of the Green's function (which correspond to the propagating modes) with respect to the orthonormal basis of $L^2(0, D)$ that is formed by the vertical eigenfunctions X_n, i.e.,

$$\widehat{G}_n(z_a, \cdot) = \int_0^D \widehat{G}((z_a, x'), \cdot) \, X_n(x') \, dx'. \tag{12}$$

Proof. See Appendix A. ∎

The passive imaging functional. Motivated by Proposition 3.1 we define here our imaging functional for the passive case. Assuming that the array elements are dense enough, so that we may think of the array as being continuous, we define

$$\widehat{\mathbb{Q}}_n = \int_0^D \widehat{\Pi}\big(\vec{\boldsymbol{x}}_r;\omega\big) X_n(x)\,dx, \quad n = 1,\dots,M, \tag{13}$$

to be the projection of the recorded field on the first M eigenfunctions X_n, $n = 1,\dots,M$, of the vertical eigenvalue problem (5). We note that the definition of $\widehat{\mathbb{Q}}_n$ in (13) entails an idealized continuous array; this is convenient mainly for theoretical purposes. In practice, we work with arrays that consist of discrete elements, and then we may define

$$\widehat{\mathbb{Q}}_n := h\sum_{r=1}^{N} \widehat{\Pi}\big((z_a,x_r);\omega\big) X_n(x_r), \quad n = 1,\dots,M,$$

where h is the array interelement distance.

Notice that using (7), we may write $\mathbb{Q}_n$ as

$$\widehat{\mathbb{Q}}_n = \int_0^D \widehat{G}\big((z_a,x),\vec{\boldsymbol{x}}_s\big) X_n(x)\,dx = \widehat{G}_n(z_a,\vec{\boldsymbol{x}}_s).$$

In view of (11) we define our imaging functional as

$$\mathcal{I}^{\mathrm{P}}(\vec{\boldsymbol{y}}^s) := \sum_{n=1}^{M} \beta_n \overline{\widehat{\mathbb{Q}}_n}\, \widehat{G}_n(z_a,\vec{\boldsymbol{y}}^s). \tag{14}$$

Note that the evaluation of $\mathcal{I}^{\mathrm{P}}(\vec{\boldsymbol{y}}^s)$, for $\vec{\boldsymbol{y}}^s \in \mathcal{S}$, requires only recordings of the wave field. Moreover, (10) and (11) ensure that

$$\mathcal{I}^{\mathrm{P}}(\vec{\boldsymbol{y}}^s) = \operatorname{Im}\widehat{G}(\vec{\boldsymbol{y}}^{\mathrm{s}},\vec{\boldsymbol{x}}_s). \tag{15}$$

This last equation is a very interesting result and says that the quality of the focusing in the image is determined by the imaginary part of the Green's function in our waveguide. Therefore, a resolution analysis for $\mathcal{I}^{\mathrm{P}}$ will entail the study of the behavior of $\operatorname{Im}\widehat{G}$.

Example 3.2 (imaging a point source). In order to provide the reader with a sense of how $\mathcal{I}^{\mathrm{P}}(\vec{\boldsymbol{y}}^{\mathrm{s}})$ behaves, we consider the simple case of imaging a source in a homogeneous terminating waveguide that forms a semi-infinite strip, i.e., $\Omega = (-\infty,R)\times(0,D)$. We assume a reference wavenumber $k_0 = \pi/10$ that corresponds to a reference wavelength λ_0 and take $D = 10\lambda_0$, while the vertical (terminating) boundary is placed at $R = 27.5\lambda_0$. In Figure 3, we plot the modulus of (14) for a source placed at $\vec{\boldsymbol{x}}_s = (19,5)\lambda_0$ (shown in the plot as a white asterisk) and for a single frequency f that corresponds to a wavenumber $k = 0.973k_0$. This results in a number of propagating modes $M = 19$. Finally, our search domain is $\mathcal{S} = [11.5,26.5]\times[0,10]$, where all distances are expressed in terms of the reference wavelength λ_0.

We observe that the $\mathcal{I}^{\mathrm{P}}(\vec{\boldsymbol{y}}^{\mathrm{s}})$ image, despite the presence of relatively high secondary peaks, displays a clear peak around $\vec{\boldsymbol{x}}_s$, which is a key property for an imaging functional.

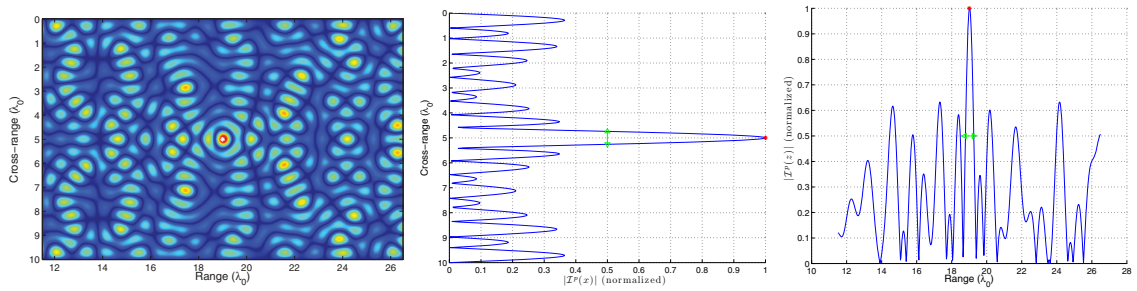

Figure 3. *Normalized modulus of $\mathcal{I}^p$ for a point source located at $\vec{\boldsymbol{x}}_s = (19, 5)\,\lambda_0$ and for a single frequency corresponding to $k = 0.973k_0$. Imaging on the whole search domain (left), for search points fixed at the correct range $z = z_s$ (middle), and at the correct cross-range $x = x_s$ (right). The green arrows indicate length equal to $\lambda/2$, and a red asterisk points to the location of the source.*

3.1.2. Active imaging. As a step toward the general case of an extended scatterer, we will now deal with the active imaging problem where we are interested in locating a single point scatterer of unit reflectivity that is situated at $\vec{\boldsymbol{x}}^* = (z^*, x^*)$, while the array $\mathcal{A}$ is like the one in the passive imaging case as illustrated in Figure 4.

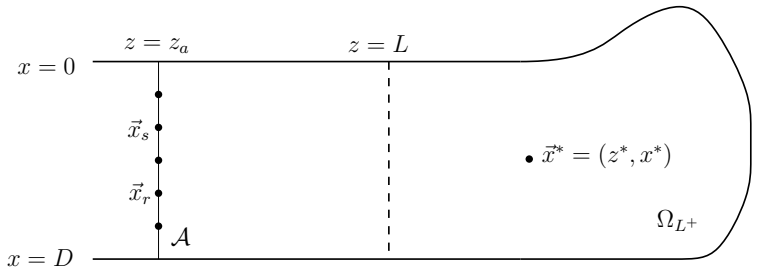

Figure 4. *Active imaging setup in a terminated waveguide.*

Then, the (s, r) entry of the array response matrix,

$$\widehat{\Pi}(\vec{\boldsymbol{x}}_s, \vec{\boldsymbol{x}}_r; \omega) = k^2 \widehat{G}(\vec{\boldsymbol{x}}^*, \vec{\boldsymbol{x}}_s; \omega) \widehat{G}(\vec{\boldsymbol{x}}_r, \vec{\boldsymbol{x}}^*; \omega),$$

corresponds to the scattered signal received at $\vec{\boldsymbol{x}}_r$ when the point reflector at x^* is illuminated by a unit amplitude signal emitted at frequency ω from a point source located at $\vec{\boldsymbol{x}}_s$. In what follows we suppress the multiplicative constant k^2, and hence we assume that

$$\widehat{\Pi}(\vec{\boldsymbol{x}}_s, \vec{\boldsymbol{x}}_r; \omega) = \widehat{G}(\vec{\boldsymbol{x}}^*, \vec{\boldsymbol{x}}_s; \omega) \widehat{G}(\vec{\boldsymbol{x}}_r, \vec{\boldsymbol{x}}^*; \omega). \tag{16}$$

In the multiple frequency case we can also remove this factor by rescaling the data matrix $\widehat{\Pi}(\vec{\boldsymbol{x}}_s, \vec{\boldsymbol{x}}_r; \omega)$ to be equal to $k^{-2}\widehat{\Pi}(\vec{\boldsymbol{x}}_s, \vec{\boldsymbol{x}}_r; \omega)$.

Assuming again that the array is continuous, we define the projected response matrix $\widehat{\mathbb{Q}}$ as

$$\widehat{\mathbb{Q}}_{nm} = \int_0^D \int_0^D \widehat{\Pi}(\vec{\boldsymbol{x}}_s, \vec{\boldsymbol{x}}_r; \omega) X_n(x_s) X_m(x_r)\, dx_s\, dx_r, \quad n, m = 1, \ldots, M, \tag{17}$$

where, as before, X_n, $n = 1, \ldots, M$, are the first M eigenfunctions of problem (5).

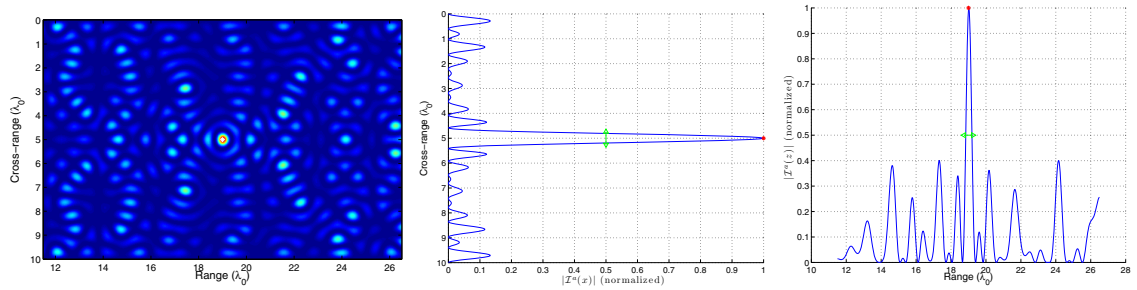

Figure 5. *Normalized modulus of $\mathcal{I}^{\mathrm{a}}$ for a point scatterer located at $\vec{\boldsymbol{x}}^* = (19, 5)\,\lambda_0$ and for a single frequency corresponding to $k = 0.973k_0$. Imaging on the whole search domain (left), for search points fixed at the correct range $z = z^*$ (middle), and at the correct cross-range $x = x^*$ (right). The green arrows indicate length equal to $\lambda/2$, and a red asterisk points to the location of the scatterer.*

The active imaging functional. A natural generalization of the imaging functional that we have proposed in the passive case is the active imaging functional

$$\mathcal{I}^{\mathrm{a}}(\vec{\boldsymbol{y}}^{\mathrm{s}}) := \sum_{n=1}^{M}\sum_{m=1}^{M} \beta_n\beta_m \overline{\widehat{\mathbb{Q}}_{nm}}\, \widehat{G}_n(z_a, \vec{\boldsymbol{y}}^{\mathrm{s}})\, \widehat{G}_m(z_a, \vec{\boldsymbol{y}}^{\mathrm{s}}), \tag{18}$$

defined for each point $\vec{\boldsymbol{y}}^{\mathrm{s}}$ in the search domain S.

Note that by substituting (16) into (17) and using the expression of $\widehat{G}_n$ given in (12), it is easy to show that

$$\widehat{\mathbb{Q}}_{nm} = \widehat{G}_n(z_a, \vec{\boldsymbol{x}}^*)\, \widehat{G}_m(z_a, \vec{\boldsymbol{x}}^*). \tag{19}$$

In turn, (18) now becomes

$$\mathcal{I}^{\mathrm{a}}(\vec{\boldsymbol{y}}^{\mathrm{s}}) = \sum_{n=1}^{M} \beta_n\, \overline{\widehat{G}_n(z_a, \vec{\boldsymbol{x}}^*)}\, \widehat{G}_n(z_a, \vec{\boldsymbol{y}}^{\mathrm{s}}) \sum_{m=1}^{M} \beta_m\, \overline{\widehat{G}_m(z_a, \vec{\boldsymbol{x}}^*)}\, \widehat{G}_m(z_a, \vec{\boldsymbol{y}}^{\mathrm{s}}),$$

and Proposition 3.1 ensures that

$$\mathcal{I}^{\mathrm{a}}(\vec{\boldsymbol{y}}^{\mathrm{s}}) = \Big(\operatorname{Im} \widehat{G}(\vec{\boldsymbol{y}}^{\mathrm{s}}, \vec{\boldsymbol{x}}^*)\Big)^2. \tag{20}$$

Thus we deduce that the imaging functional (18) for a point scatterer behaves like the square of the imaginary part of the Green's function.

Example 3.3 (imaging a point scatterer). To illustrate how $\mathcal{I}^{\mathrm{a}}(\vec{\boldsymbol{y}}^{\mathrm{s}})$ behaves we consider a point scatterer in the homogeneous terminating waveguide that we described in Example 3.2. The scatterer is placed at $\vec{\boldsymbol{x}}^* = (19, 5)\,\lambda_0$, while all the other parameters are as in the previous example. In Figure 5 we plot the modulus of (18). As one may immediately verify, this image has a better signal-to-noise (SNR) ratio than the one shown in Figure 3. This is something to be expected since $\mathcal{I}^{\mathrm{a}}$ is just the square of $\mathcal{I}^{\mathrm{p}}$. We note that in this work we loosely interpret the term SNR to refer to the ratio of the main peak to secondary peaks.

We conclude by noting that so far we have proven that the point spread functions in the passive and in the active imaging case are determined by the imaginary part of the Green's function when the array spans the whole vertical cross-section of the waveguide. Next, we consider the partial aperture array case and present the modifications that have to be carried out in the previous approach in order to extend its applicability in this more challenging setup.

3.2. Imaging with a partial aperture array. We now turn our attention to the case where the array does not span the whole vertical cross-section of the waveguide. In [31] we presented a way to construct a projection of the array response matrix that is well suited to that case. Here we briefly describe the basic idea, necessary notation, and main results that appear in [31] in order to apply them in our current setup.

Let A_{arr} be the $M \times M$ matrix with entries

$$(A_{\text{arr}})_{mn} = \int_{\mathcal{A}} X_m(x) X_n(x) \mathrm{d}x, \quad m, n = 1, \ldots, M, \tag{21}$$

where M is the number of propagating modes in Ω_{L^-}. We have shown that A_{arr} is a real, symmetric Toeplitz-minus-Hankel matrix, and its eigenvalues ν_j, $j = 1, \ldots, M$, are clustered near 0 and 1; in fact if l_{arr} is the length of the array $\mathcal{A}$, then approximately $[l_{\text{arr}}/(\lambda/2)]$ of the ν_i's lie near 1, and the rest $M - [l_{\text{arr}}/(\lambda/2)]$ are approaching zero. Let also $\boldsymbol{w}^j = (w_1^j, w_2^j, \ldots, w_M^j)^T$ be the corresponding orthonormal eigenvectors, which turn out to be discrete prolate (or prolate-like) spheroidal sequences, and let W be the $M \times M$ orthogonal matrix $W = (\boldsymbol{w}^1, \boldsymbol{w}^2, \ldots, \boldsymbol{w}^M)$. Then we introduce the trigonometric polynomials

$$s_j(x) = \sum_{i=1}^{M} w_i^j X_i(x), \quad j = 1, 2, \ldots, M. \tag{22}$$

Next, we project $\widehat{\Pi}$ onto the first M trigonometric polynomials s_n, $n = 1, \ldots, M$, instead of onto the eigenfunctions X_n. Specifically, we define $\widehat{\mathbb{S}}$ to be the $M \times M$ matrix with entries

$$\widehat{\mathbb{S}}_{mn} = \frac{1}{\nu_m \nu_n} \int_{\mathcal{A}} \int_{\mathcal{A}} \widehat{\Pi}(\vec{\boldsymbol{x}}_s, \vec{\boldsymbol{x}}_r, \omega)\, s_m(x_s)\, s_n(x_r)\, dx_s\, dx_r, \quad m, n = 1, \ldots, M. \tag{23}$$

It is easy to check that

$$\int_{\mathcal{A}} s_k(x) X_m(x)\, dx = \nu_k\, w_m^k, \quad k, m = 1, \ldots, M. \tag{24}$$

Finally, we define $\widehat{\mathbb{Q}}$ as

$$\widehat{\mathbb{Q}} = W\, \widehat{\mathbb{S}}\, W^T. \tag{25}$$

For implementation aspects of this approach and for an extensive discussion on its performance, we refer the reader to [31]. Notice that in the case of an array with full aperture the matrix A_{arr} is just the identity matrix, $s_j(x) = X_j(x)$ and $W = I_M$, and thus we recover the definition of $\mathbb{Q}$ given in (17).

The following proposition shows that in the case of a point scatterer (active imaging) when we use (23) and (25) to construct the matrix $\widehat{\mathbb{Q}}$ we practically recover the same data as if we were working with a full aperture array.

Proposition 3.4. *Let a single point scatterer of unit reflectivity be located at* $\vec{\boldsymbol{x}}^* = (z^*, x^*) \in \Omega_{L^+}$ *(see Figure 4). We assume that the array* $\mathcal{A}$ *is at range* $z = z_a \ll L$*, so that the evanescent part of the wave field may be neglected. Then the projected array response matrix* $\widehat{\mathbb{Q}}$ *defined by (23) and (25) for a partial aperture array is equal to the projected matrix* $\widehat{\mathbb{Q}}$ *for an array that spans the whole vertical cross-section* $[0, D]$*.*

Proof. For a single point scatterer the (s, r) entry of the array response matrix $\widehat{\Pi}$ is given by $\widehat{\Pi}(\vec{\boldsymbol{x}}_s, \vec{\boldsymbol{x}}_r) = \widehat{G}(\vec{\boldsymbol{x}}^*, \vec{\boldsymbol{x}}_s)\widehat{G}(\vec{\boldsymbol{x}}_r, \vec{\boldsymbol{x}}^*)$; see (16). Moreover, note that for each $\vec{\boldsymbol{x}} = (z, x) \in \Omega_{L^-}$ that satisfies the assumption $z \ll L$, the Green's function may be written as

$$\widehat{G}(\vec{\boldsymbol{x}}, \vec{\boldsymbol{x}}^*) \approx \sum_{i=1}^{M} C_i X_i(x), \tag{26}$$

since the evanescent modes can be neglected for large propagation distances. Obviously $C_i = \widehat{G}_i(z, \vec{\boldsymbol{x}}^*)$, where $\widehat{G}_i(\cdot, \vec{\boldsymbol{x}}^*)$ is defined in (12).

In the full aperture array case the orthonormality of the X_n's immediately implies that $\widehat{\mathbb{Q}}_{nm} = C_n C_m$; see also (19).

If the array has partial aperture, then (23) implies that

$$\begin{aligned}
\widehat{\mathbb{S}}_{nm} &= \frac{1}{\nu_n \nu_m} \int_{\mathcal{A}} \int_{\mathcal{A}} \widehat{G}(\vec{\boldsymbol{x}}^*, \vec{\boldsymbol{x}}_s)\, \widehat{G}(\vec{\boldsymbol{x}}_r, \vec{\boldsymbol{x}}^*)\, s_n(x_s)\, s_m(x_r)\, dx_s dx_r \\
&= \frac{1}{\nu_n \nu_m} \sum_{k=1}^{M} \sum_{l=1}^{M} C_k C_l \int_{\mathcal{A}} s_n(x_s) X_k(x_s) dx_s \int_{\mathcal{A}} s_m(x_r) X_l(x_r) dx_r \\
&\overset{(24)}{=} \sum_{k=1}^{M} C_k w_k^n \sum_{l=1}^{M} C_l w_l^m.
\end{aligned}$$

Hence

$$\begin{aligned}
\widehat{\mathbb{Q}}_{nm} &\overset{(25)}{=} (W \widehat{\mathbb{S}} W^T)_{nm} = \sum_{j=1}^{M} w_n^j \sum_{i=1}^{M} s_{ji} w_m^i = \sum_{j=1}^{M} w_n^j \sum_{i=1}^{M} \sum_{k=1}^{M} \sum_{l=1}^{M} C_k C_l w_k^j w_l^i w_m^i \\
&= \sum_{k=1}^{M} \sum_{l=1}^{M} C_k C_l \sum_{j=1}^{M} w_n^j w_k^j \sum_{i=1}^{M} w_l^i w_m^i = \sum_{k=1}^{M} \sum_{l=1}^{M} C_k C_l (W W^T)_{nk} (W W^T)_{lm} \\
&= C_n C_m,
\end{aligned}$$

where the last equality holds since W is orthogonal. ∎

Remark 3.5.

(a) An analogous result to that stated in Proposition 3.4 is expected to hold also for extended scatterers under the linearized Born approximation.

(b) Proposition 3.4 essentially says that when the array has partial aperture and we construct $\widehat{\mathbb{Q}}$ by means of (23) and (25), we do not lose any information, and the resulting image is expected to be as good as if the array were spanning the whole vertical cross-section of the waveguide. Of course, this holds ideally assuming, e.g., that the array

is continuous and that all necessary computations are performed "exactly," i.e., with infinite precision. However, our analysis in [31] suggests that the minimum eigenvalue $\nu_{\min}$ of A_{arr} decays to zero as the length of the array decreases. As a result, numerical instabilities occur when the length of the array is decreased, so that some of the smaller-in-magnitude eigenvalues drop below some small-valued threshold ϵ, which may depend on the noise level in the data or on the machine epsilon in the noiseless case. In such a case, we propose to filter the matrix $\widehat{\mathbb{S}}$ by setting $1/\nu_i = 0$ for those indices i that correspond to eigenvalues ν_i that satisfy $\nu_i < \epsilon$. For the details we refer the reader to [31].

(c) In the case of reflectors that are in the vicinity of the array, we may include a number of evanescent terms in the expansion (26) and adjust appropriately the size of the matrices A_{arr}, $\widehat{\mathbb{S}}$, and $\widehat{\mathbb{Q}}$.

In the case of passive imaging with a partial aperture array, our methodology is modified as follows: We first construct the vector $\widehat{\mathbb{S}}$ with entries

$$\widehat{\mathbb{S}}_n = \frac{1}{\nu_n} \int_{\mathcal{A}} \widehat{\Pi}(\vec{\boldsymbol{x}}_r)\, s_n(x_r)\, dx_r, \quad n = 1, \ldots, M, \tag{27}$$

and then we define the vector

$$\widehat{\mathbb{Q}} = W\widehat{\mathbb{S}}, \tag{28}$$

where the matrix W is as before. It is straightforward to show that the projected array response vector $\widehat{\mathbb{Q}}$ for a continuous array that spans the whole vertical cross-section $[0, D]$ is equal to the vector defined by (27) and (28) in the case of a partial aperture array.

We conclude this section by proposing the following imaging algorithms for imaging one or more extended sources or scatterers located in Ω_{L^+}.

Algorithm 3.6 (passive imaging).

(a) Given the $N \times 1$ array response vector $\widehat{\Pi}$ we compute the $M \times 1$ projected vector $\widehat{\mathbb{Q}}$ by means of (27) and (28).

(b) Next, we compute the imaging functional $\mathcal{I}^{\text{p}}$ given in (14) for each point of a predefined search domain S, and we display graphically the modulus of these values.

Algorithm 3.7 (active imaging).

(a) Given the $N \times N$ array response matrix $\widehat{\Pi}$ we compute the $M \times M$ projected matrix $\widehat{\mathbb{Q}}$ by means of (23) and (25).

(b) Next, we compute the imaging functional $\mathcal{I}^{\text{a}}$ given in (18) for each point of a predefined search domain S, and we display graphically the modulus of these values.

4. Resolution analysis. In this section we present a detailed resolution analysis for the imaging functionals $\mathcal{I}^{\text{p}}$ and $\mathcal{I}^{\text{a}}$ defined in (14) and (18), respectively. As usual, this amounts to studying the behavior of the point spread function (PSF) which is the imaging functional for a point source (passive case) or a point scatterer (active case). In fact, we are going to examine only the case of a point source since the results of the previous section ensure that the PSF for a point scatterer is just the square of the PSF for a point source.

Specifically, we restrict ourselves to the simple case of a homogeneous waveguide ($\eta(\vec{\boldsymbol{x}}) = 1$) which forms the semi-infinite strip $(-\infty, R) \times (0, D)$. The Green's function in this waveguide, hereafter denoted by $\widehat{G}^R$, may be found analytically; the derivation is given in Appendix B. We have that for each $\vec{\boldsymbol{y}}^{\mathrm{s}} = (z, x) \in \Omega$,

$$\widehat{G}^R(\vec{\boldsymbol{y}}^s, \vec{\boldsymbol{x}}_s) = \begin{cases} \displaystyle\sum_{m=1}^{\infty} \frac{1}{\beta_m} \mathrm{e}^{i\beta_m(R-z_s)} \sin\beta_m(R-z)\, X_m(x)\, X_m(x_s), & z > z_s, \\ \displaystyle\sum_{m=1}^{\infty} \frac{1}{\beta_m} \mathrm{e}^{i\beta_m(R-z)} \sin\beta_m(R-z_s)\, X_m(x)\, X_m(x_s), & z < z_s, \end{cases} \tag{29}$$

where the point source is located at $\vec{\boldsymbol{x}}_s = (z_s, x_s)$, the vertical eigenpairs (μ_n, X_n) are equal to

$$\mu_n = (n\pi/D)^2, \quad X_n(x) = \sqrt{2/D}\sin(\sqrt{\mu_n}x), \ n = 1, 2, \ldots, \tag{30}$$

and the horizontal wavenumbers β_n are defined in (6).

Then, as (15) suggests, the PSF for a point source is

$$\begin{aligned} \mathcal{I}^{\mathrm{p}}(\vec{\boldsymbol{y}}^{\mathrm{s}}) &= \operatorname{Im}\widehat{G}^R(\vec{\boldsymbol{y}}^{\mathrm{s}}, \vec{\boldsymbol{x}}_s) = \sum_{n=1}^{M} \frac{1}{\beta_n} \sin\beta_n(R-z_s) \sin\beta_n(R-z)\, X_n(x)\, X_n(x_s) \\ &= \frac{1}{2}\sum_{n=1}^{M} \frac{1}{\beta_n}\Big(\cos\beta_n(z-z_s) - \cos\beta_n(2R-z-z_s)\Big) X_n(x)\, X_n(x_s). \end{aligned} \tag{31}$$

4.1. Single frequency. The analysis in this subsection will be carried out for a monochromatic source. The following two propositions provide analytical estimates of the PSF when we fix the range or the cross-range to that of the point source and look at a cross-section in the other direction.

Proposition 4.1 (cross-range resolution). *Assume that the search point is located at the correct range, i.e., $\vec{\boldsymbol{y}}^{\mathrm{s}} = (z_s, x)$. Then, for M sufficiently large, it holds that*

$$\mathcal{I}^{\mathrm{p}}(z_s, x) \approx \tfrac{1}{4}\left[\big(J_0(\alpha_x) - J_0(\beta_x)\big) - \big(J_0(\sqrt{\alpha_x^2+\gamma_x^2}) - J_0(\sqrt{\beta_x^2+\gamma_x^2})\big)\right], \tag{32}$$

where

$$\alpha_x = \frac{2\pi(x-x_s)}{\lambda}, \quad \beta_x = \frac{2\pi(x+x_s)}{\lambda}, \quad \gamma_x = \frac{4\pi}{\lambda}(R-z_s). \tag{33}$$

Proof. For $\vec{\boldsymbol{y}}^{\mathrm{s}} = (z_s, x)$, and in view of (30), (31) becomes

$$\mathcal{I}^{\mathrm{p}}(z_s, x) = \frac{1}{D}\sum_{n=1}^{M} \frac{1}{\beta_n}\Big(1 - \cos(2\beta_n(R-z_s))\Big) \sin\frac{n\pi x}{D} \sin\frac{n\pi x_s}{D}. \tag{34}$$

Letting $\xi_n = n\lambda/(2D)$, we may view the right-hand side of (34) as a Riemann sum approximation of the integral

$$\frac{1}{\pi}\int_0^1 \frac{1}{\sqrt{1-\xi_n^2}}\Big(1 - \cos\Big(\frac{4\pi}{\lambda}(R-z_s)\sqrt{1-\xi_n^2}\Big)\Big) \sin\Big(\frac{2\pi x}{\lambda}\xi_n\Big) \sin\Big(\frac{2\pi x_s}{\lambda}\xi_n\Big) d\xi_n.$$

Hence, using the simple trigonometric identity $\sin A \sin B = \frac{1}{2}(\cos(A-B) - \cos(A+B))$, we may approximate $\mathcal{I}^{\mathrm{p}}$ as

$$\mathcal{I}^{\mathrm{p}}(x) \approx \frac{1}{\pi}\int_0^1 \frac{1}{\sqrt{1-\xi_n^2}}\Big(1-\cos\Big(\frac{4\pi}{\lambda}(R-z_s)\sqrt{1-\xi_n^2}\Big)\Big) \times \frac{1}{2}\Big(\cos\Big(\frac{2\pi(x-x_s)}{\lambda}\xi_n\Big) - \cos\Big(\frac{2\pi(x+x_s)}{\lambda}\xi_n\Big)\Big)\, d\xi_n,$$

where we have slightly extended the notation and used $\mathcal{I}^{\mathrm{p}}$ here as a function of a single variable (cross-range). Now, with α_x, β_x, and γ_x given by (33), $\mathcal{I}^{\mathrm{p}}$ can be written as

$$\begin{aligned}
\mathcal{I}^{\mathrm{p}}(x) &\approx \frac{1}{2\pi}\int_0^1 \frac{1}{\sqrt{1-\xi_n^2}}\Big(1-\cos\big(\gamma_x\sqrt{1-\xi_n^2}\big)\Big)\Big(\cos(\alpha_x\xi_n) - \cos(\beta_x\xi_n)\Big)\, d\xi_n \\
&= \frac{1}{2\pi}\int_0^1 \frac{1}{\sqrt{1-\xi_n^2}}\cos(\alpha_x\xi_n)\, d\xi_n - \frac{1}{2\pi}\int_0^1 \frac{1}{\sqrt{1-\xi_n^2}}\cos(\beta_x\xi_n)\, d\xi_n \\
&\quad + \frac{1}{2\pi}\int_0^1 \frac{1}{\sqrt{1-\xi_n^2}}\cos(\alpha_x\xi_n)\cos\big(\gamma_x\sqrt{1-\xi_n^2}\big)\, d\xi_n \\
&\quad - \frac{1}{2\pi}\int_0^1 \frac{1}{\sqrt{1-\xi_n^2}}\cos(\beta_x\xi_n)\cos\big(\gamma_x\sqrt{1-\xi_n^2}\big)\, d\xi_n \\
&=: I_1 - I_2 + I_3 - I_4. \qquad (35)
\end{aligned}$$

The integrals I_i, $i = 1, \ldots, 4$, in (35) may be evaluated analytically. We look at each term separately. For example, it is known, [16, eq. (3.753.2)], that

$$\int_0^1 \frac{1}{\sqrt{1-\xi_n^2}}\cos(\alpha_x\xi_n)\, d\xi_n = \frac{\pi}{2}J_0(\alpha_x),$$

where $J_0(\cdot)$ is the Bessel function of the first kind of order 0. Therefore,

$$I_1 = \frac{1}{4}J_0(\alpha_x) \quad \text{and} \quad I_2 = \frac{1}{4}J_0(\beta_x).$$

Next, in order to evaluate I_3 we change variables, letting $\theta = \arcsin\xi_n$, and use the fact that $J_{-1/2}(t) = \sqrt{\frac{2}{\pi t}}\cos(t)$ (see, e.g., [26, eq. (10.16.1)]) to write I_3 as

$$I_3 = \frac{1}{4}\sqrt{\alpha_x\gamma_x}\int_0^{\pi/2} J_{-1/2}(\alpha_x\sin\theta)J_{-1/2}(\gamma_x\cos\theta)(\sin\theta)^{1/2}(\cos\theta)^{1/2}d\theta.$$

Then, according to [16, eq. (6.683.2)], $I_3 = \frac{1}{4}J_0(\sqrt{\alpha_x^2+\gamma_x^2})$. Similarly, $I_4 = \frac{1}{4}J_0(\sqrt{\beta_x^2+\gamma_x^2})$, and the proof is complete. ∎

Proposition 4.2 (range resolution). *Assume that the search point is located at the correct cross-range, i.e., $\vec{\boldsymbol{y}}^{\mathrm{s}} = (z, x_s)$. Then, for M sufficiently large, it holds that*

$$\mathcal{I}^{\mathrm{p}}(z, x_s) \approx \tfrac{1}{4}\Big[\big(J_0(\alpha_z) - J_0(\beta_z)\big) - \big(J_0(\sqrt{\alpha_z^2+\gamma_z^2}) - J_0(\sqrt{\beta_z^2+\gamma_z^2})\big)\Big], \qquad (36)$$

where now

$$\alpha_z = \frac{2\pi(z - z_s)}{\lambda}, \quad \beta_z = \frac{2\pi(2R - z - z_s)}{\lambda}, \quad \gamma_z = \frac{4\pi x_s}{\lambda}. \tag{37}$$

Proof. Since $\vec{\boldsymbol{y}}^s$ is placed at the correct cross-range, we now let $x = x_s$ in (31). Thus, by a slight abuse of notation, $\mathcal{I}^{\mathrm{P}}(z)$ as a function of the range variable equals

$$\mathcal{I}^{\mathrm{P}}(z) = \frac{1}{D}\sum_{n=1}^{M}\frac{1}{\beta_n}\Big(\cos\beta_n(z - z_s) - \cos\beta_n(2R - z - z_s)\Big)\,\sin^2\frac{n\pi x_s}{D}. \tag{38}$$

As in the proof of Proposition 4.1, we let $\xi_n = n\lambda/(2D)$ and approximate the right-hand side of (34) by an integral. Specifically, if $\alpha_z, \beta_z, \gamma_z$ are as in (37), and if we use that $\sin^2 A = \frac{1}{2}(1 - \cos 2A)$, we may deduce that $\mathcal{I}^{\mathrm{P}}(z)$ is approximated as

$$\begin{aligned}\mathcal{I}^{\mathrm{P}}(z) \approx \frac{1}{2\pi}\int_0^1 \frac{1}{\sqrt{1-\xi_n^2}}\big(\cos(\alpha_z\sqrt{1-\xi_n^2}) - \cos(\beta_z\sqrt{1-\xi_n^2})\big)\\ \times\big(1 - \cos(\gamma_z\xi_n)\big)\,d\xi_n.\end{aligned} \tag{39}$$

The integrals of the various terms of (39) are of the same type as those in (35) and can be evaluated analytically, resulting in (36). ∎

First, we note that the approximate formulas (32) and (36) for the PSF when range or cross-range, respectively, is fixed at the correct location of the point source suggest that the term which mainly contributes to defining the resolution in the vicinity of the source is $J_0(\alpha_x)$ or $J_0(\alpha_z)$, respectively. To illustrate this, in Figure 6 we superimpose the graphs of (32) multiplied by 4 (blue solid line) and of $J_0(a_x)$ (red dashed line) for a source located at $(z_s, x_s) = (19, 5)\,\lambda_0$ and for a single frequency corresponding to $k = 0.973k_0$. The reference wavenumber is $k_0 = \pi/10$.

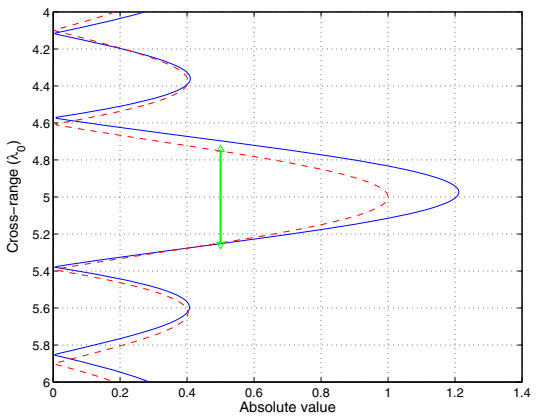

Figure 6. *Comparison between (32) multiplied by 4 (blue solid line) and $J_0(a_x)$ (red dashed line) for a source located at $(z_s, x_s) = (19, 5)\,\lambda_0$ and for a single frequency corresponding to $k = 0.973k_0$, where the reference wavenumber is $k_0 = \pi/10$. The green arrows indicate length equal to $\lambda/2$.*

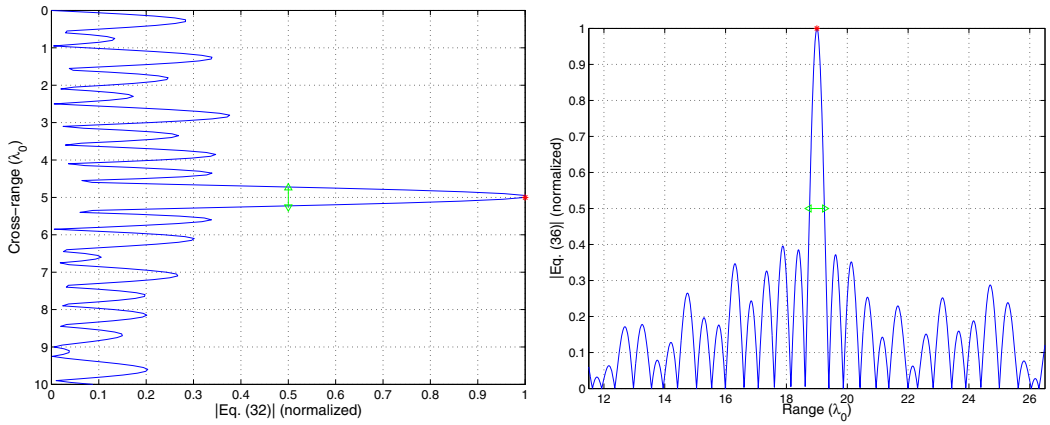

Figure 7. *Normalized absolute value of (32) versus cross-range (left subplot) and normalized absolute value of (36) versus range (right subplot) for a point source located at* $(z_s, x_s) = (19, 5)\,\lambda_0$. *Here the reference wavenumber is* $k_0 = \pi/10$, *and results are shown for a single frequency that corresponds to* $k = 0.973k_0$. *The green arrows indicate length equal to* $\lambda/2$, *and a red asterisk points to the location of the source.*

Hence, if we define the resolution to be the width of the PSF at its half maximum, it is immediate to check that both cross-range and range resolution are approximately equal to $\lambda/2$.

Next, in Figure 7 we plot the absolute values of (32) (left subplot) and (36) (right subplot) for a point source located at $(z_s, x_s) = (19, 5)\,\lambda_0$. As before, the reference wavenumber is $k_0 = \pi/10$, and results are shown for a single frequency that corresponds to $k = 0.973k_0$. The analytical expressions we have derived for the cross-range and range resolution capture the behavior of the imaging functional as we may check by comparing the plots in Figure 7 with the middle and right subplots of Figure 3. The images shown in Figures 3 and 7 peak at the right position of $\vec{\boldsymbol{x}}_s$ and, as predicted by the theoretical analysis, they have a resolution of $\lambda/2$ in both range and cross-range directions. We observe, however, that they are quite oscillatory and that their SNR is not very satisfactory.

4.2. Multiple frequencies. In this subsection we will show that the SNR in our images can be significantly improved using multiple frequencies. For most practical purposes, this is something feasible since in many applications sources are not monochromatic but rather emit pulses. The multiple frequency version of the imaging functional defined in (14) is simply the summation over frequencies of the corresponding monochromatic functional,

$$\mathcal{I}^{\mathrm{P}}(\vec{\boldsymbol{y}}^s) := \sum_{l=1}^{N_f} \mathcal{I}^{\mathrm{P}}(\vec{\boldsymbol{y}}^s; f_l) = \sum_{l=1}^{N_f} \sum_{n=1}^{M_l} \beta_n(f_l) \overline{\widehat{\mathbb{P}}_n}(f_l)\, \widehat{G}_n(z_a, \vec{\boldsymbol{y}}^s; f_l), \tag{40}$$

where f_l, $l = 1, \ldots, N_f$, are the discrete frequencies that span the available frequency interval $[f_{\min}, f_{\max}]$ in our data. Note that M_l depends on the index l since the number of propagating modes depends on the frequency f_l. The definition of the corresponding active imaging functional for multiple frequencies follows similarly.

Let us first look at the cross-range direction. To investigate the PSF behavior with multiple frequencies in the ideal setting that we have examined thus far, we integrate (32) with respect

to frequency f over an interval with bandwidth B. Specifically, letting $\Psi(x;B)$ denote the PSF for multiple frequencies at the correct range, we have

$$\begin{aligned}\Psi(x;B) &= \int_{f_{\min}}^{f_{\max}} \mathcal{I}^{\mathrm{p}}(z_s,x;f)df \\ &\approx \tfrac{1}{4}\int_{f_{\min}}^{f_{\max}} \Big[\big(J_0(\alpha_x)-J_0(\beta_x)\big)-\big(J_0(\sqrt{\alpha_x^2+\gamma_x^2})-J_0(\sqrt{\beta_x^2+\gamma_x^2})\big)\Big]\,df \\ &\approx \tfrac{1}{4}\int_{f_{\min}}^{f_{\max}} J_0(\alpha_x)\,df, \qquad (41)\end{aligned}$$

where now the parameters α_x, β_x, and γ_x (given in (33)) are written in terms of the frequency f as

$$\alpha_x = \frac{2\pi}{c_0}(x-x_s)f, \quad \beta_x = \frac{2\pi}{c_0}(x+x_s)f, \quad \gamma_x = \frac{4\pi(R-z_s)}{c_0}f,$$

where c_0 is the constant wave speed, f_c is the central frequency, and $[f_{\min}, f_{\max}] = [f_c - \frac{B}{2}, f_c + \frac{B}{2}]$. Note that we have numerically verified the validity of the last approximation in (41) at least in the frequency range that we have examined. Now, let $\zeta_x := \frac{2\pi}{c_0}(x-x_s)$. Then [1, 11.1.7],

$$\Psi(x;B) \approx \frac{1}{4}\int_{f_{\min}}^{f_{\max}} J_0(\zeta_x f)\,df = \frac{1}{4\zeta_x}\Big(\Lambda_0\big(\zeta_x f_{\max}\big)-\Lambda_0\big(\zeta_x f_{\min}\big)\Big), \qquad (42)$$

where

$$\Lambda_0(s) := sJ_0(s) + \frac{\pi s}{2}\Big(J_1(s)\mathbf{H}_0(s) - J_0(s)\mathbf{H}_1(s)\Big), \qquad (43)$$

$J_n(\cdot)$ is the Bessel function of the first kind of order n, and $\mathbf{H}_n(\cdot)$, is the Struve function of order n, respectively. (For the definition of the Struve function see, e.g., [1, Chap. 12].)

Let us consider a specific example. Assume a point source located at $(z_s, x_s) = (19, 5)\lambda_0$, a reference wavenumber equal to $k_0 = \pi/10$, and a central frequency f_c corresponding to $k_c = 0.973k_0$. In Figure 8 we superimpose the modulus of the right-hand side of (42) for three different bandwidths that are equal to $B = 10\%$, 50%, and 100% of the central frequency f_c. All three are normalized with respect to their maximum value which, as may be immediately inferred from (42), is equal to $B/4$. Moreover, we observe that resolution is determined by the central frequency, while SNR is improved as the bandwidth increases. Specifically, when $B = 0.10f_c$ the SNR seems to be of the same order as in the single frequency case (compare the blue dashed-dotted line with the blue solid line in the left plot of Figure 7), it is slightly improved when $B = 0.50f_c$, and it is considerably improved by a factor of 2 for the larger bandwidth $B = f_c$. Let us quantify these observations. Obviously the global maximum of $|\Psi(x;B)|$ is attained at $x = x_s$ and is equal to $B/4$. Then, for the bandwidths considered in the example referring to Figure 8, the SNR is determined as the ratio of the maximum value to the second taller peak; assume that the latter is attained at $\rho(B)$. Hence (42) and (43)

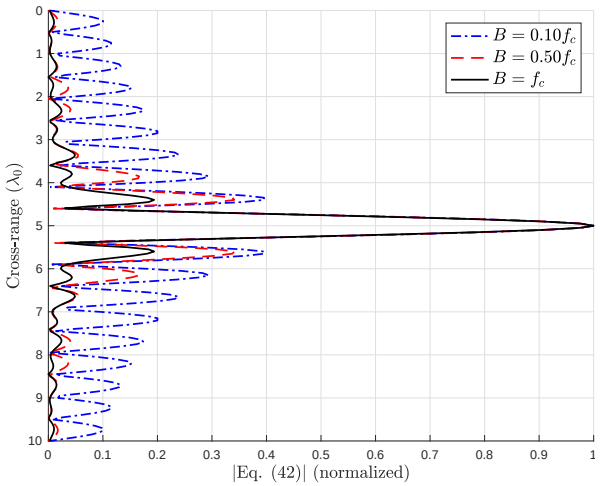

Figure 8. *Modulus of (42) for bandwidth equal to $B = 0.10f_c$ (blue dashed-dotted line), $B = 0.50f_c$ (red dashed line), and $B = 1.00f_c$ (black solid line). The point source is placed at $(z_s, x_s) = (19, 5)\lambda_0$, the reference wavenumber is $k_0 = \pi/10$, and the central frequency f_c corresponds to $k = 0.973k_0$.*

imply that $\zeta_\rho := \frac{2\pi}{c_0}(\rho(B) - x_s)$ satisfies the following equation:

$$\begin{aligned} &f_{\max}\Big(J_1(\zeta_\rho f_{\max})\mathbf{H}_0(\zeta_\rho f_{\max}) - J_0(\zeta_\rho f_{\max})\mathbf{H}_1(\zeta_\rho f_{\max})\Big) \\ &-f_{\min}\Big(J_1(\zeta_\rho f_{\min})\mathbf{H}_0(\zeta_\rho f_{\min}) - J_0(\zeta_\rho f_{\min})\mathbf{H}_1(\zeta_\rho f_{\min})\Big) = 0. \end{aligned} \tag{44}$$

Moreover, it is immediate to check that since ζ_ρ is a root of (44), then

$$\Psi(\rho(B); B) = \frac{1}{4}\big(f_{\max}J_0(\zeta_\rho f_{\max}) - f_{\min}J_0(\zeta_\rho f_{\min})\big),$$

and hence $\mathrm{SNR} = B/|f_{\max}J_0(\zeta_\rho f_{\max}) - f_{\min}J_0(\zeta_\rho f_{\min})|$.

We compute numerically $\rho(B)$ for the various bandwidths reported above, and our results are summarized in Table 1.

Table 1
SNR in cross-range for various bandwidths.

B	$\rho(B)$	SNR
$0.10f_c$	$5.62521\lambda_0$	2.4981
$0.50f_c$	$5.61865\lambda_0$	2.9097
$1.00f_c$	$5.59433\lambda_0$	5.1513

The situation in the range direction is completely the same, so we do not present it here.

We observe the same behavior when we work with the actual imaging functional $\mathcal{I}^{\mathrm{P}}$. For example, in Figure 9 we plot the modulus of $\mathcal{I}^{\mathrm{P}}(\vec{\boldsymbol{y}}^{\mathrm{S}})$ for a point source located (as before) at $(z_s, x_s) = (19, 5)\lambda_0$, a reference wavenumber equal to $k_0 = \pi/10$, and a central frequency f_c that corresponds to $k_c = 0.973k_0$. The left image is obtained when the bandwidth $B \approx 0.15f_c$ and the middle image when $B \approx 0.51f_c$, and the right image corresponds to $B = 0.92f_c$. The

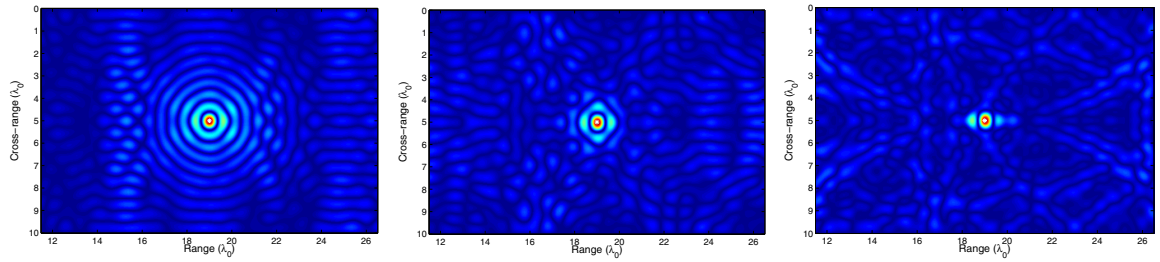

Figure 9. *Imaging with $\mathcal{I}^{\mathrm{p}}$ for multiple frequencies for a point source placed at $(z_s, x_s) = (19, 5)\lambda_0$. The reference wavenumber equals $k_0 = \pi/10$, and the central frequency f_c corresponds to $k_c = 0.973k_0$. Left: Bandwidth $B = 0.15f_c$. Middle: $B = 0.51f_c$. Right: $B = 0.92f_c$.*

advantage of using multiple frequencies is evident when we compare these images with the left plot of Figure 3. Moreover, using a bandwidth of the same order as the central frequency greatly improves the SNR in the right plot of Figure 9.

Finally, in Figure 10 we plot the $(\mathrm{Im}\,\widehat{G}^R(\vec{\boldsymbol{y}}^{\mathrm{s}}; \vec{\boldsymbol{x}}_s))^2$ which, as (20) suggests, is equal to $\mathcal{I}^{\mathrm{a}}(\vec{\boldsymbol{y}}^{\mathrm{s}})$. We examine the same cases as in Figure 9 and, while the noise levels are lower even at the single frequency case (compare with the left plot in Figure 5), again have a clear SNR improvement as the bandwidth increases. As we will see in the next section, this effect is of greater importance when one deals with extended scatterers.

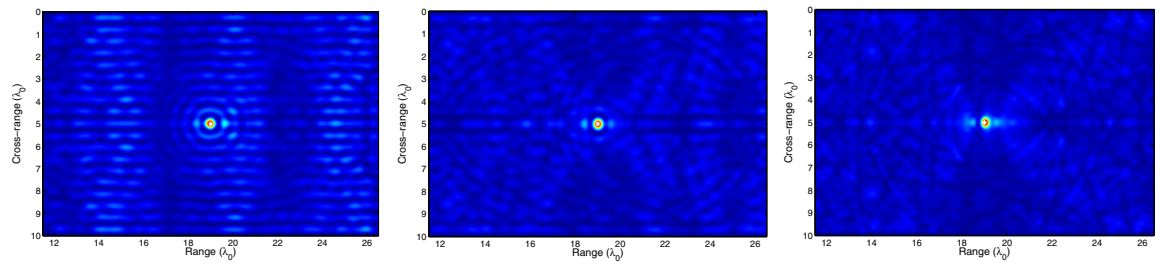

Figure 10. *Imaging with $\mathcal{I}^{\mathrm{a}}$ for multiple frequencies for a point scatterer placed at $(z_s, x_s) = (19, 5)\lambda_0$. The central frequency f_c is the same as in Figure 9. Left: Bandwidth $B = 0.15f_c$. Middle: $B = 0.51f_c$. Right: $B = 0.92f_c$.*

To summarize, in this section we derived analytical formulas that approximate the PSF for a point source in cross-range and range. We have concluded that both range and cross-range resolution equal $\lambda/2$ in the monochromatic case. Moreover, we addressed the improvement in SNR when using multiple frequencies, and we have shown that the resolution in the multiple frequency case is $\lambda_c/2$, where λ_c is the wavelength that corresponds to the central frequency of the available bandwidth. We note that the resolution analysis carries over to the partial aperture case at least for array apertures such that the minimum eigenvalue $\nu_{\min}$ of A_{arr} is larger than ϵ (see Remark 3.5).

5. Numerical experiments.

In this section we focus on the active imaging case and assess the performance of $\mathcal{I}^{\mathrm{a}}$ for imaging extended reflectors in terminating waveguides. We start with a model problem for which the scattered data is computed using the linearized Born

approximation and then consider several extended reflectors for which the scattered data is computed by solving the full wave equation. In all cases we will show imaging results obtained using $\mathcal{I}^{\mathrm{a}}$ with multiple frequencies. We first show numerical results for a full aperture array and then consider the more challenging case of a partial aperture array.

5.1. Linearized Born scattered data. We consider a one-dimensional scatterer $\mathcal{C}$, which is a semicircle placed in a homogeneous waveguide with flat horizontal boundaries and a vertical terminating boundary at $z = R$, i.e., $\Omega = (-\infty, R) \times (0, D)$. The response matrix is computed using the Born approximation and is given by

$$\widehat{\Pi}(\vec{\boldsymbol{x}}_s, \vec{\boldsymbol{x}}_r; \omega) = \int_{\mathcal{C}} \widehat{G}^R(\vec{\boldsymbol{x}}, \vec{\boldsymbol{x}}_s; \omega) \widehat{G}^R(\vec{\boldsymbol{x}}_r, \vec{\boldsymbol{x}}; \omega) d\vec{\boldsymbol{x}}, \tag{45}$$

with $\widehat{G}^R(\vec{\boldsymbol{x}}, \vec{\boldsymbol{y}}; \omega)$ as in (29). Note that in (45) we have suppressed the multiplicative factor k^2 that usually appears in its right-hand side. As already mentioned in subsection 3.1.2, this can be performed in practice by rescaling the data matrix $\widehat{\Pi}(\vec{\boldsymbol{x}}_s, \vec{\boldsymbol{x}}_r; \omega)$ as $k^{-2}\widehat{\Pi}(\vec{\boldsymbol{x}}_s, \vec{\boldsymbol{x}}_r; \omega)$.

Recall also that our imaging functional $\mathcal{I}^{\mathrm{a}}$ is given by

$$\mathcal{I}^{\mathrm{a}}(\vec{\boldsymbol{y}}^{\mathrm{s}}) = \sum_{l=1}^{N_f} \sum_{n=1}^{M_l} \sum_{m=1}^{M_l} \beta_n(f_l)\beta_m(f_l) \overline{\widehat{\mathbb{Q}}_{nm}(f_l)}\, \widehat{G}_n^R(z_a, \vec{\boldsymbol{y}}^{\mathrm{s}}; f_l)\, \widehat{G}_m^R(z_a, \vec{\boldsymbol{y}}^{\mathrm{s}}; f_l), \tag{46}$$

where $\widehat{\mathbb{Q}}$ is the projected array response matrix (see (23) and (25)) and $\widehat{G}_n^R$, $n = 1, \ldots, M_l$, is the projection of the Green's function on the first M_l vertical eigenfunctions; cf. (12). To demonstrate the effect of the terminating boundary of the waveguide on imaging, we compare the results obtained when the same reflector is placed in a terminating and in an open-ended (infinite-strip) waveguide. For both the open-ended and the terminating waveguide the array is placed at $z_a = 0$ and spans the whole vertical cross-section of the waveguide. The semicircular scatterer $\mathcal{C}$ is centered at $(z^*, x^*) = (19, 5)\lambda_0$ with diameter $b = 2\lambda_0$, and we use frequencies $f \in [f_c - B/2, f_c + B/2]$, where the central frequency f_c corresponds to the wavenumber $k_c = 0.975k_0$, the reference wavenumber, as before, equals $k_0 = \pi/10$, and the bandwidth is equal to $B = 0.92f_c$. For the terminating waveguide, the vertical boundary is placed at $R = 27.5\lambda_0$.

To compute the data and the image for the open-ended waveguide, we simply replace $\widehat{G}^R(\vec{\boldsymbol{y}}, \vec{\boldsymbol{x}}_s; \omega)$ in (45) and (46) by the Green's function for the infinite waveguide, hereafter denoted by $\widehat{G}^0(\vec{\boldsymbol{y}}, \vec{\boldsymbol{x}}_s; \omega)$. Recall that $\widehat{G}^0$ is given by (see, e.g., [19])

$$\widehat{G}^0(\vec{\boldsymbol{y}}, \vec{\boldsymbol{x}}_s; \omega) = \frac{i}{2} \sum_{m=1}^{\infty} \frac{1}{\beta_m} \mathrm{e}^{i\beta_m|z-z_s|}\, X_m(x)\, X_m(x_s), \tag{47}$$

where $\vec{\boldsymbol{y}} = (z, x) \in \Omega$ and $\vec{\boldsymbol{x}}_s = (z_s, x_s)$, the vertical eigenpairs (μ_n, X_n) are as in (30), and the horizontal wavenumbers β_n are defined in (6).

In Figure 11 we plot the modulus of $\mathcal{I}^{\mathrm{a}}$ for the case of an open-ended waveguide (plots shown in the first and third columns) and a terminating waveguide (second and fourth columns). We have used two different bandwidths. The images shown in the first and second columns were obtained with bandwidth $B = 0.51f_c$, while B was taken equal to $B = 0.92f_c$

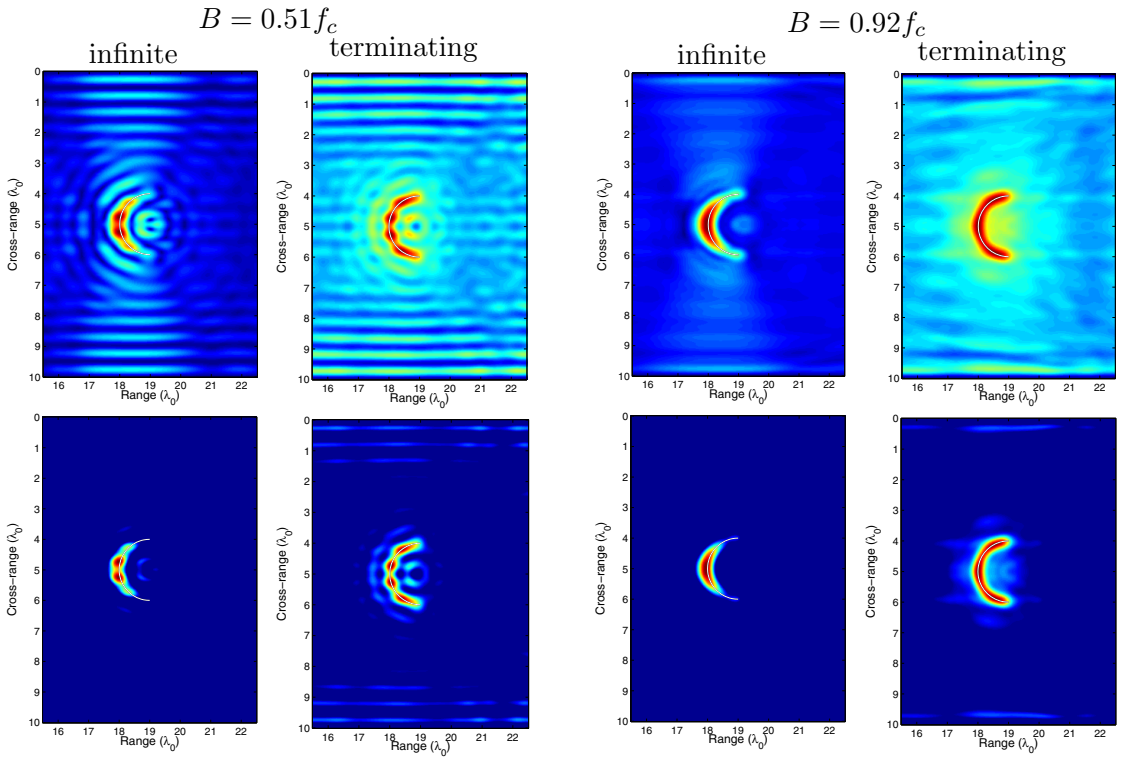

Figure 11. *Multiple frequency imaging with $\mathcal{I}^{\mathrm{a}}$ of a semicircular reflector centered at $(z^*, x^*) = (19, 5)\lambda_0$. Specifically, $f \in [f_c - B/2, f_c + B/2]$ with $k_c = 0.975k_0$, $k_0 = \pi/10$. For the first two columns the bandwidth is equal to $B = 0.51f_c$, while a larger bandwidth $B = 0.92f_c$ is used for the two columns on the right. The images shown in the first and third columns correspond to the open-ended waveguide, while those depicted in the second and fourth correspond to the terminating waveguide. In the top row we plot the modulus of the image normalized by its maximum value, while in the bottom row we use a threshold that sets to zero the values of the image with normalized modulus less than $\ell = 0.4$.*

for the images shown in the third and fourth columns. These results are in perfect agreement with our theoretical analysis which suggests that SNR improves as we increase the bandwidth. In the remaining part of this section we fix the bandwidth to $B = 0.92f_c$. In all plots, the image is normalized with respect to its maximum value. Looking carefully at the images in Figure 11, we observe that those in the open-ended waveguide exhibit a lower noise compared to the corresponding ones in the terminating waveguide, while the latter offer a better reconstruction of the entire scatterer shape compared to those in the infinite waveguide, which focus mainly around the midpoint of the semicircle. This can be seen more clearly in the images displayed in the bottom row, where we threshold the normalized modulus of the image values that are less than $\ell = 0.4$. From now on we will refer to this process as thresholding with parameter ℓ.

5.2. Full wave scattered data. Next, we want to test our approach in imaging extended scatterers without using any simplifying approximation for the forward model. To this end, we now construct the array response matrix $\widehat{\Pi}$ by solving the wave equation (1) numerically, with the aid of the high-order finite element C++ code Montjoie [24]. The originally semi-

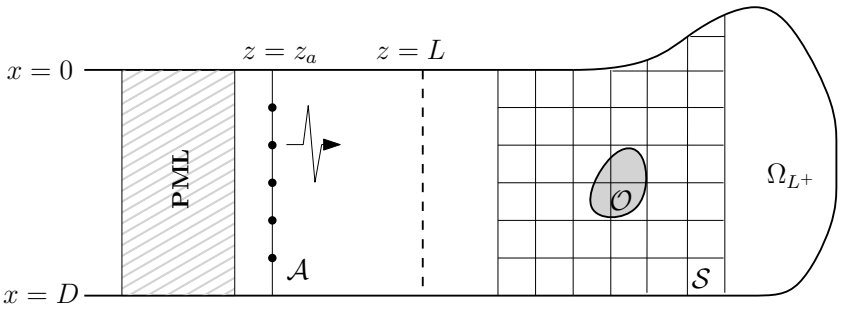

Figure 12. *Sketch of a waveguide that is truncated near the array with a PML.*

infinite waveguide is truncated with a perfectly matched layer (PML), as shown in Figure 12, that ranges between $-5\lambda_0$ and 0, a width sufficient to absorb waves propagating to $-\infty$. We discretize the finite computational domain using quadrangles, in which we use $\mathbb{Q}_{12}$ polynomials ($\mathbb{Q}_n = \text{span}\{x^l y^m,\ 0 \le l, m \le n\}$), while we use a fourth-order leapfrog scheme for the time domain discretization.

The array imaging setup is similar to the one used in the previous subsection, with the exception that now our vertical array is placed at $z_a = 2\lambda_0$ and has a pitch $h = \lambda_0/4$. First, we consider the case of the semi-infinite strip, i.e., $\Omega = (-\infty, R) \times (0, D)$, where now the terminating vertical boundary is located at $R = 28\lambda_0$ and a disc-shaped scatterer of diameter $b = 2\lambda_0$ is centered at $(z^*, x^*) = (20.5, 5)\lambda_0$. A Neumann condition is imposed on the circular boundary of the scatterer. In the right subplot of Figure 13(a) (second image in the panel) we plot the modulus of $\mathcal{I}^a$ normalized by its maximum value. As one may immediately verify, even though the SNR of the image is a bit low, the location, size, and shape of the scatterer are fully recovered. For the image in the left subplot (first image in the panel) we pretend that we are not aware that the waveguide has a closed end, and we back propagate the same data with the "wrong" Green's function, i.e., the one for the open-ended waveguide. We implement this by replacing in (46) the terms $\widehat{G}_m^R$, $\widehat{G}_n^R$ by $\widehat{G}_m^0$, $\widehat{G}_n^0$, respectively, i.e., by the Fourier coefficients of the Green's function for the infinite waveguide (see (47)) with respect to the orthonormal basis $\{X_n\}_{n=1}^{\infty}$ of $L^2(0, D)$. As a result, only the left part of the scatterer is recovered. In an attempt to improve the SNR of these images, in Figure 13(b) we plot the corresponding images after thresholding with $\ell = 0.4$.

As a second example, we place in the previously described waveguide a rhombus-shaped scatterer of diameter $b = 2\lambda_0$, centered at $(z^*, x^*) = (20.5, 3)\lambda_0$. Figure 14 is analogous to Figure 13. As before, in the left subplot of each subfigure we present the image obtained when we back propagate our data with the Green's function for the open-ended waveguide; again we observe that only the left part of the scatterer can be reconstructed. When we use the correct Green's function, the corresponding image in the right subplot of each subfigure exhibits a good reconstruction of the scatterer.

Finally, to demonstrate the robustness and the generality of our imaging approach we consider a waveguide Ω with a more complex geometry. Specifically, the waveguide has constant width in the cross-range direction equal to $10\lambda_0$ until $z = 17\lambda_0$, and then it expands vertically by $2\lambda_0$ on both sides and keeps a new constant width of $14\lambda_0$ until it is terminated by a

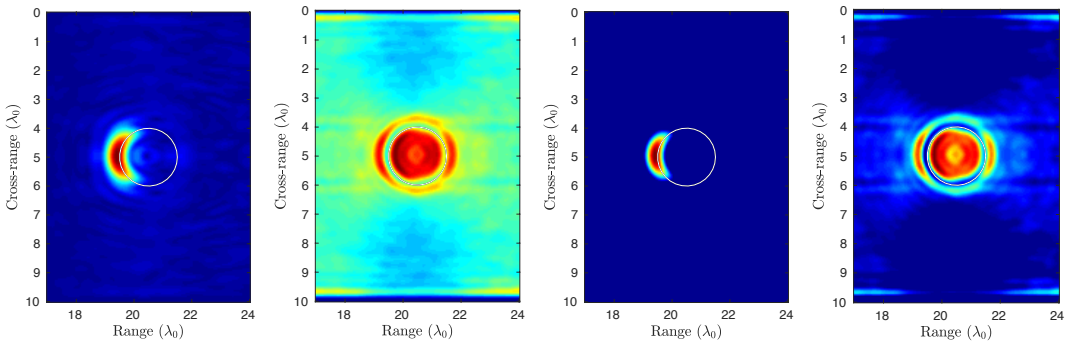

(a) No threshold used. (b) Threshold equal to 0.4.

Figure 13. *Imaging with $\mathcal{I}^{\mathrm{a}}$ of a disc-shaped scatterer centered at $(z^*, x^*) = (20.5, 5)\lambda_0$, for $k_c = 0.9733k_0$, $k_0 = \pi/10$, and $B = 0.92f_c$.* (a) *Data is back propagated with the Green's function for the open-ended (left subplot) and the terminating waveguide (right subplot), where we do not use thresholding.* (b) *Same setup as in* (a) *but using thresholding with $\ell = 0.4$.*

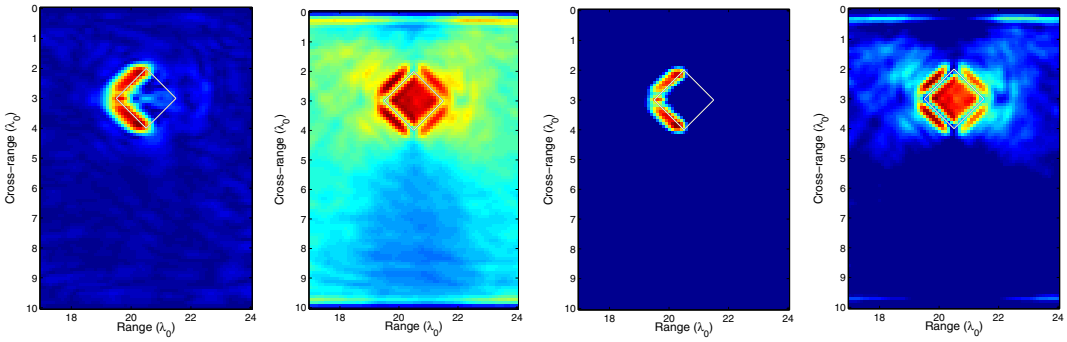

(a) No threshold used. (b) Threshold equal to 0.4.

Figure 14. *Imaging with $\mathcal{I}^{\mathrm{a}}$ of a rhombus-shaped scatterer centered at $(z^*, x^*) = (20.5, 3)\lambda_0$, for $k_c = 0.9733k_0$, $k_0 = \pi/10$, and $B = 0.92f_c$.* (a) *Data is back propagated with the Green's function for the open-ended (left subplot) and the terminating waveguide (right subplot), where we do not use thresholding.* (b) *Same setup as in* (a) *but using thresholding with $\ell = 0.4$.*

vertical boundary located at $z = 28\lambda_0$. The geometry of part of the waveguide is depicted in the imaging results shown in Figure 15. A disc-shaped scatterer with diameter $b = 2\lambda_0$ is centered at $(z^*, x^*) = (22.5, 7)\lambda_0$ and is depicted in Figure 15 with a white continuous line.

For this waveguide geometry, we do not have an analytic expression for the Green's function $\widehat{G}(\vec{\boldsymbol{y}}^s, \vec{\boldsymbol{x}}_s)$, which is needed to form the image; hence we compute it numerically. To be more precise, $\widehat{G}(\vec{\boldsymbol{y}}^s, \vec{\boldsymbol{x}}_s)$ is obtained by solving the wave equation in Ω in the absence of the scatterer for all sources' locations $\vec{\boldsymbol{x}}_s$, $s = 1, \ldots, N$, and the solution is stored for all search points $\vec{\boldsymbol{y}}^s$ in the imaging window. The computations are performed in the time domain, and we use FFT to transform the data in the frequency domain.

The imaging results are shown in Figure 15 where we plot on the left the normalized modulus of $\mathcal{I}^{\mathrm{a}}$ without a threshold, and on the right using a threshold $\ell = 0.4$. The reconstruction

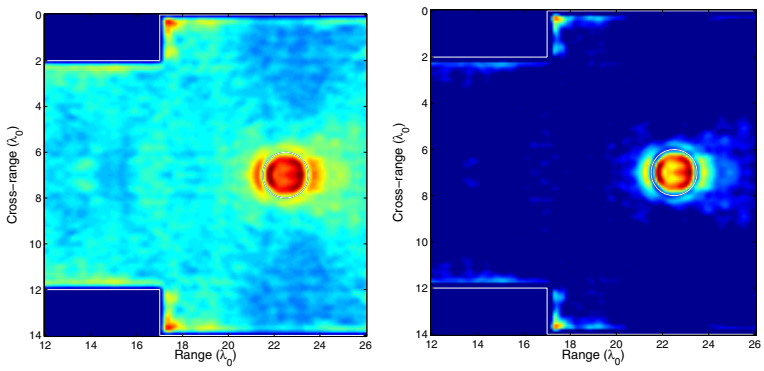

Figure 15. *Imaging with $\mathcal{I}^{\rm a}$ for a disc scatterer centered at $(z^*, x^*) = (22.5, 7)\lambda_0$, for $k_c = 0.9733k_0$, $k_0 = \pi/10$, and $B = 0.92f_c$. On the left we use no threshold, while on the right we have a threshold $\ell = 0.4$.*

is successful since it provides good estimates for the size and shape of the reflector.

5.3. Imaging with partial aperture. We consider now the more challenging problem of imaging a reflector with an array that does not span the entire vertical cross-section of the waveguide. As we have described in Algorithm 3.7, our imaging method requires the evaluation of the functional $\mathcal{I}^{\rm a}$ in each point of the search domain. Recall that in the case of multiple frequencies, $\mathcal{I}^{\rm a}$ is given in (46), and note that this expression applies for any array aperture size. What alters is the way we construct the $M_l \times M_l$ modal projected matrix $\mathbb{Q}$, which in the case of a partial aperture array uses the trigonometric polynomials s_j, $j = 1, \ldots, M_l$, as in (23) and (25) that account for the partial array aperture through the eigenvectors of the array matrix $A_{\rm arr}$.

We show in Figures 16 and 17 imaging results obtained for the same configurations as in Figures 13 and 15, respectively. The difference is that here we consider array apertures $|\mathcal{A}| = 0.75D$, $0.5D$, and $0.25D$, where D is the total width of the waveguide in the cross-range direction. As illustrated in these figures, the image quality deteriorates as the array aperture decreases but only rather moderately. Indeed, comparing these images with the corresponding ones in Figure 13, one may confirm that the images for $|\mathcal{A}| = 0.75D$ are almost indistinguishable from the full aperture ones, and they are still quite good for $|\mathcal{A}| = 0.25D$!

Next, we present an example of the performance of our algorithm under the effect of measurement noise. Specifically, we consider the waveguide environment and the circular scatterer that concern the results shown in Figure 13. We model measurement noise as in [5] by adding to the response matrix $\widehat{\Pi}$ a noise matrix $W(\omega) \in \mathbb{C}^{N\times N}$ with entries that are normally distributed with mean zero and variance $\epsilon p_{\rm avg}$. Here ϵ is a positive constant and $p_{\rm avg}$ denotes the average power received per source, receiver, and frequency. Then it turns out that the normalized noise power in dB is equal to $-10\log_{10}\epsilon$. For details of the implementation we refer the reader to [30]. In Figure 18, we present our results for two noise levels: 10 dB, shown in the top row, and 0 dB, shown in the bottom. The length of the array decreases from full aperture (leftmost column panel) to $|\mathcal{A}| = 0.25D$ (rightmost column panel). In all plots we use a threshold $\ell = 0.4$. Comparing these images with the analogous ones in Figure 16, where there is no noise, we observe that noise for both levels does not seem to affect the quality of

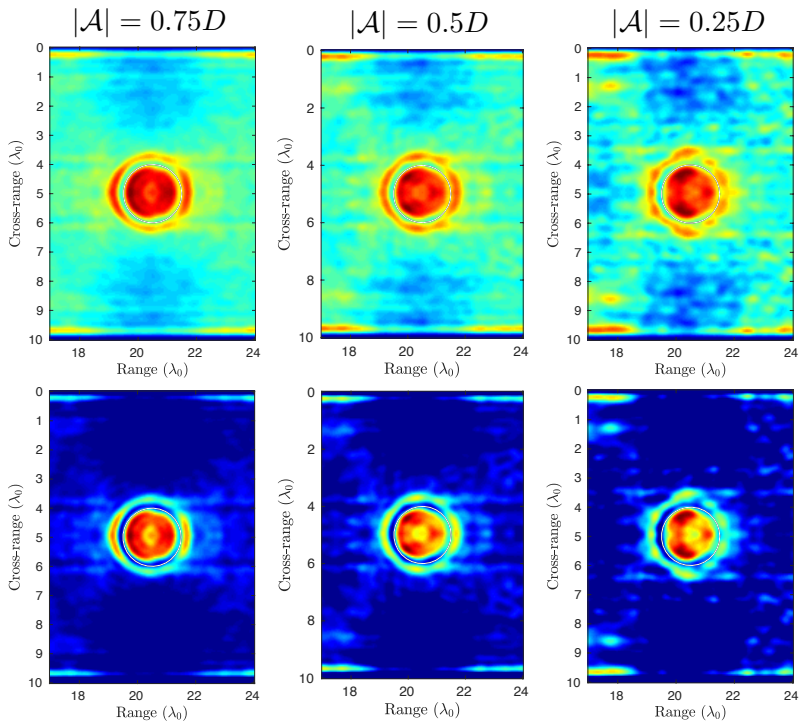

Figure 16. *From left to right: Imaging with $\mathcal{I}^{\mathrm{a}}$ for a disc scatterer centered at $(z^*, x^*) = (21.5, 5)\lambda_0$ for different array apertures $|\mathcal{A}| = 0.75D$, $0.5D$, and $0.25D$, for $k_c = 0.9733k_0$, $k_0 = \pi/10$, and $B = 0.92f_c$. In the top row of plots we use no threshold, while for the plots in the bottom row we have a threshold $\ell = 0.4$.*

the images. Note that the 0 dB level corresponds to very noisy data since in this case the power of the noise is equal to the power of the signal. These results illustrate the robustness of the proposed imaging methodology to uncorrelated measurement noise. For similar results concerning the case of an infinite waveguide with a full aperture array, we refer the reader to [30].

To synopsize, our numerical results indicate that the imaging method based on $\mathcal{I}^{\mathrm{a}}$ can be used for reconstructing extended scatterers that are located in terminating waveguides of complex geometry. The data used is the usual array response matrix, which may cover only part of the vertical cross-section of the waveguide. The array response matrix is then projected on the propagating modes in an adequate way using the trigonometric polynomials on the array aperture as in (23) and (25). We note that the same procedure can be followed for synthetic aperture data collected by a single transmit/receive element. In the latter case the data consists only of the diagonal entries of the array response matrix. We have numerically observed that the image resolution remains the same in this case, while the SNR is worse; this is expected since the number of measurements is reduced to N for the synthetic aperture instead of N^2 tabulated in the array response matrix. As an example, we show in Figure 19 full and partial aperture imaging results for the same imaging configuration as in Figure 16 but with a synthetic aperture that is formed with a single transmit/receive element.

Note that to form the image with $\mathcal{I}^{\mathrm{a}}$ we need the Green's function in the semi-infinite

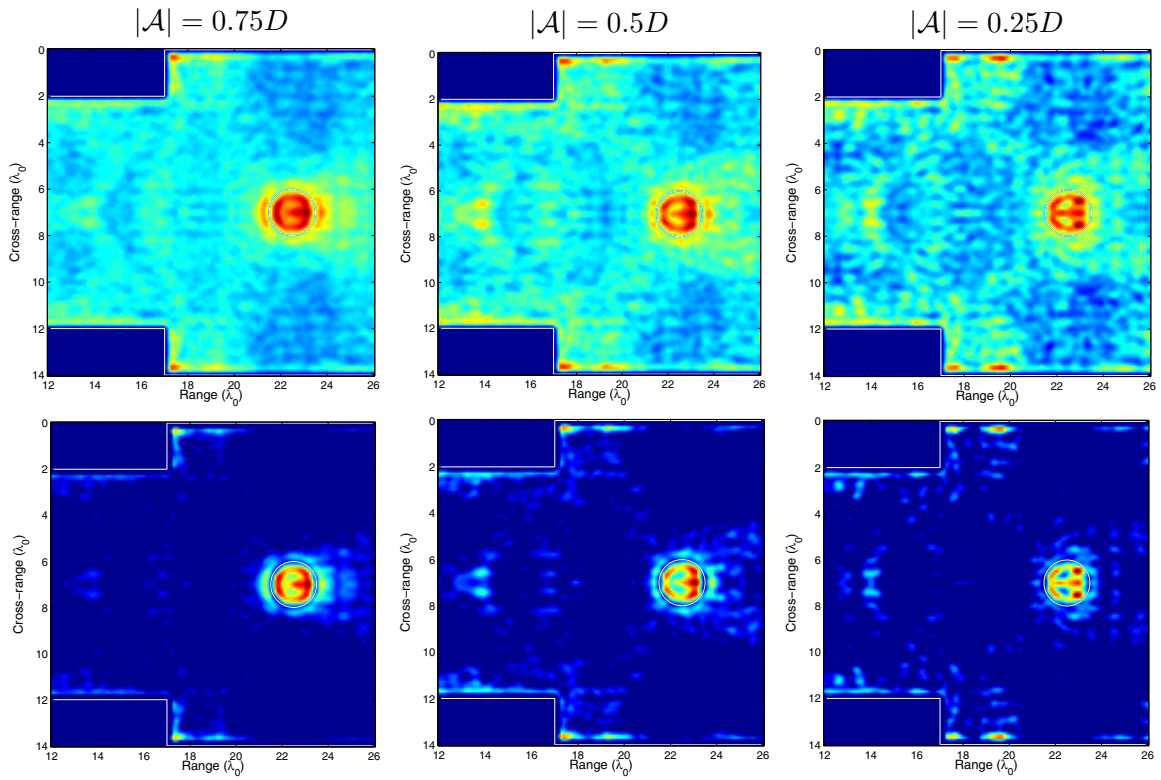

Figure 17. *From left to right: Imaging with $\mathcal{I}^{\mathrm{a}}$ for a disc scatterer centered at $(z^*, x^*) = (22.5, 7)\lambda_0$ for different array apertures $|\mathcal{A}| = 0.75D$, $0.5D$, and $0.25D$, for $k_c = 0.9733k_0$, $k_0 = \pi/10$, and $B = 0.92f_c$. In the top row of plots we use no threshold, while for the plots in the bottom row we have a threshold $\ell = 0.4$.*

waveguide, which can be computed numerically assuming that the geometry and background velocity in the waveguide are known. This is necessary for complex geometries and/or propagation media, in which case it is not possible to derive an analytical expression for the Green's function. We have also assessed the performance of the imaging method with fully nonlinear scattering data and in the presence of additive uncorrelated measurement noise.

5.4. Imaging in a three-dimensional terminating waveguide. Finally, we consider the problem of imaging an extended reflector in a three-dimensional terminating waveguide with a bounded rectangular cross-section. The imaging setup is illustrated in Figure 20. Our notation is as before, with z the range variable and x, y the two cross-range variables. The vertical cross-section of the waveguide (xy-plane) is the rectangle $(0, D) \times (0, Y)$, and the terminating boundary is at $z = R$. Homogeneous Dirichlet boundary conditions are imposed on all of the waveguide's boundaries.

For a homogeneous waveguide with a simple geometry, such as the one in Figure 20, the analytic expression for the Green's function in the waveguide may be retrieved in a straightforward way from the analogous two-dimensional expressions. Consequently, the linearized scattered acoustic field may be computed on the array of receivers $\mathcal{A}$ that span the bounded cross-section of the waveguide. Imaging is performed by the functional $\mathcal{I}^{\mathrm{a}}$ as in (18), with the projected response matrix $\widehat{\mathbb{Q}}$ defined by adequately modifying (17) so that the integrals are taken over the two-dimensional array aperture.

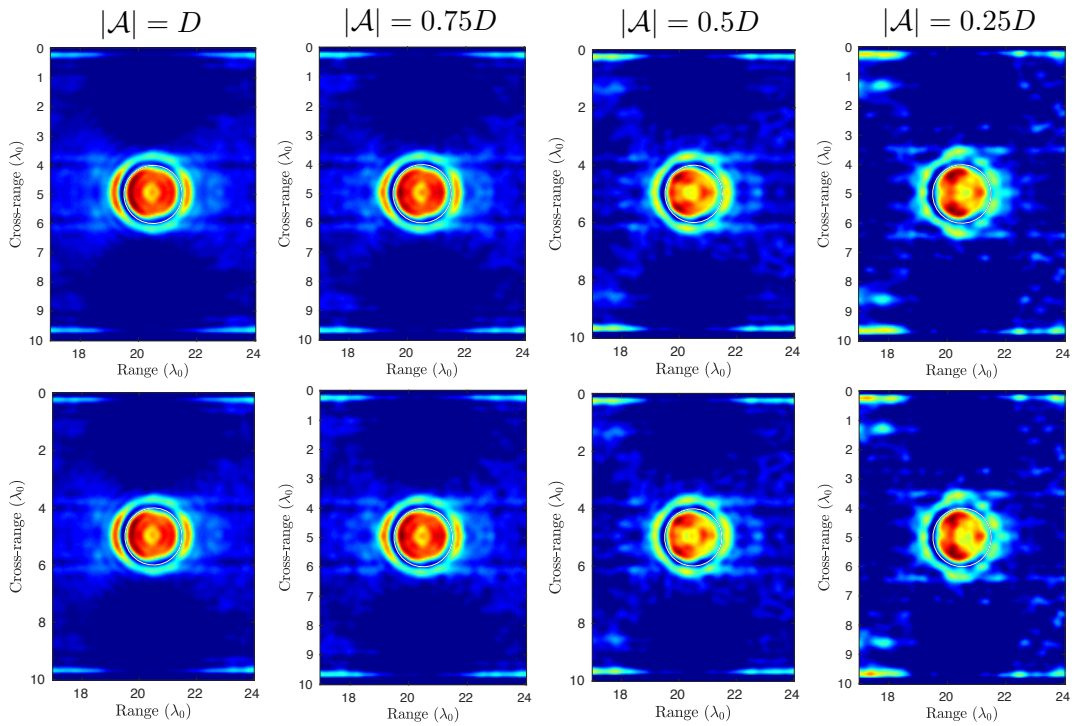

Figure 18. *From left to right: Imaging with $\mathcal{I}^{\mathrm{a}}$ for noisy measurements for a disc scatterer centered at $(z^*, x^*) = (21.5, 5)\lambda_0$ for different array apertures $|\mathcal{A}| = D,\ 0.75D,\ 0.5D,$ and $0.25D$, for $k_c = 0.9733k_0$, $k_0 = \pi/10$, and $B = 0.92f_c$. The normalized noise power $-10\log_{10}\epsilon$ is equal to 10 dB in the top row and 0 dB in the bottom row. In all plots, we have a threshold $\ell = 0.4$.*

Without giving details of the computations, in the following figures we present as a proof of concept some preliminary results that illustrate how this imaging methodology performs in the three-dimensional case. In Figure 21 we show the reconstruction for a point reflector located at $\vec{\boldsymbol{x}}^* = (19, 5, 10)\,\lambda_0$. The vertical cross-section has size $[0, 10\lambda_0] \times [0, 20\lambda_0]$, and the terminating boundary is placed at $z = 28\lambda_0$. This is a single frequency result for $k = 0.973k_0$ ($k_0 = \pi/10$) and essentially depicts the PSF of $\mathcal{I}^{\mathrm{a}}$ in three dimensions. We observe that the resolution is $\lambda/2$ in all directions as expected from our resolution analysis.

In Figure 22 we display the modulus of $\mathcal{I}^{\mathrm{a}}$ for a square-shaped screen reflector. We observe that the reconstructions are very good, and the shape of the reflector can be retrieved with accuracy.

A more challenging example is considered in Figure 23, where we seek to reconstruct a hemisphere with diameter $b = 2\lambda_0$, centered at $\vec{\boldsymbol{x}}^* = (19, 5, 10)\lambda_0$. The reconstruction shown in the right plot is very close to the true reflector's geometry shown in the left plot. These preliminary three-dimensional results are very promising. Of course, more experiments with full wave scattered data and noise should be carried out to fully assess the performance of the method in three dimensions. Also, we leave for future work the adequate modification of the imaging functional for the partial aperture case in three dimensions.

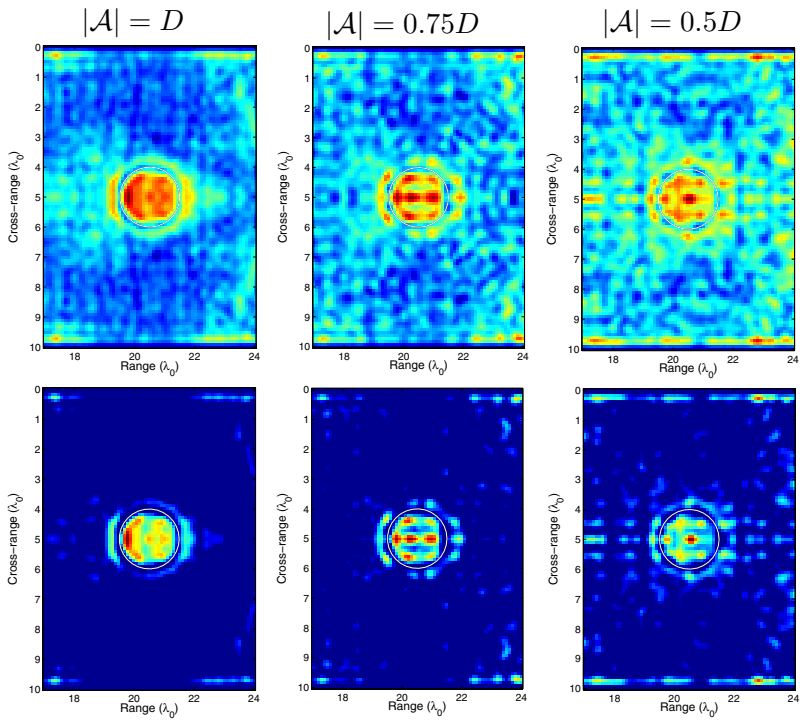

Figure 19. *From left to right: Imaging with $\mathcal{I}^a$ for a disc scatterer centered at $(z^*, x^*) = (20.5, 5)\lambda_0$ using a synthetic aperture array with length $|\mathcal{A}| = D,\ 0.75D,$ and $0.5D$, for $k_c = 0.9733k_0$, $k_0 = \pi/10$, and $B = 0.92f_c$. In the top row of plots we use no threshold, while for the plots in the bottom row we have a threshold $\ell = 0.4$.*

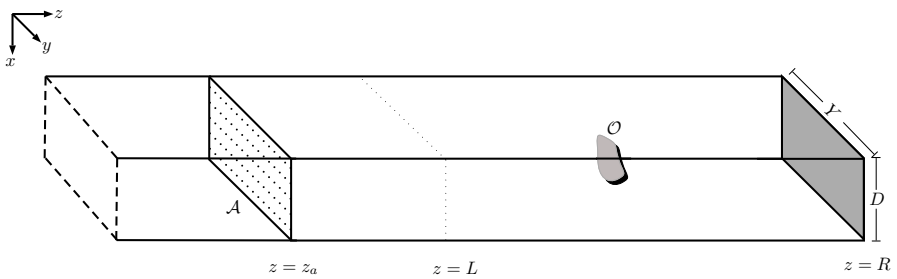

Figure 20. *Schematic representation of the imaging setup in a three-dimensional waveguide.*

6. Conclusions. We considered the problem of imaging extended reflectors in terminating waveguides $\Omega \subset \mathbb{R}^2$ that consist of two subdomains: the semi-infinite strip $\Omega_{L^-} = (-\infty, L) \times (0, D)$ and a bounded domain Ω_{L^+}. We also assume that the medium is homogeneous in the semi-infinite strip Ω_{L^-}, while it can be inhomogeneous in Ω_{L^+}, which may also contain the reflector to be imaged. This formalism allows us to image reflectors in waveguides with complex geometries. We introduce an imaging functional that relies on the back propagation of the modal projection of the array response matrix adequately defined so as to account for the array aperture. Our analysis shows that the resolution of the image is half a wave-

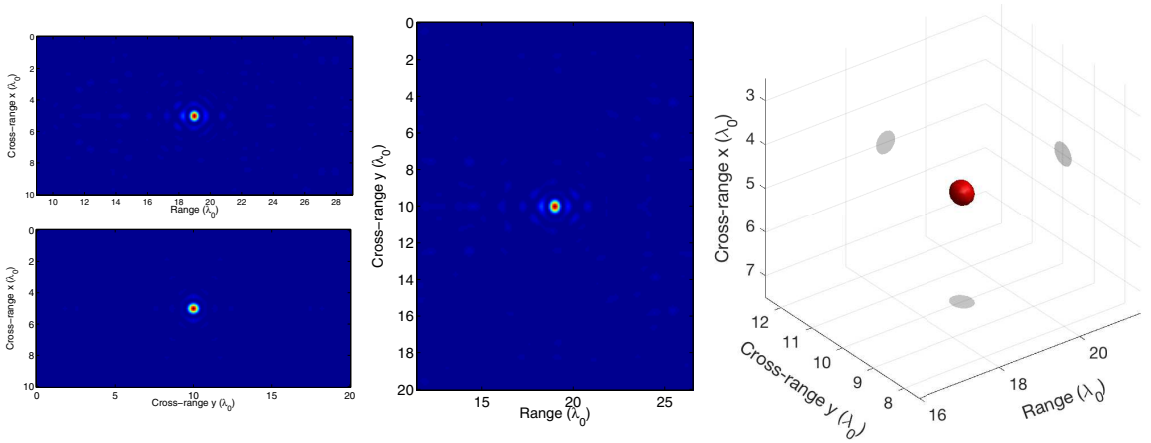

Figure 21. *Modulus of $\mathcal{I}^{\mathrm{a}}$ for the zx-plane (top left), yx-plane (bottom left), and zy-plane (middle) for a single frequency $k = 0.973k_0$, $k_0 = \pi/10$, for a point reflector placed at $\vec{\boldsymbol{x}}^* = (19, 5, 10)\ \lambda_0$. In the right plot we show the three-dimensional reconstruction of the point reflector.*

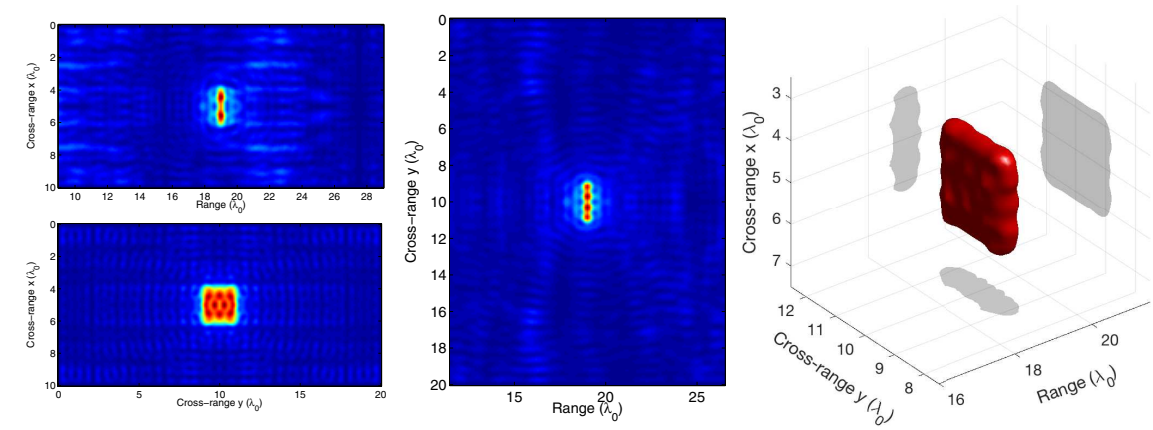

Figure 22. *Modulus of $\mathcal{I}^{\mathrm{a}}$ for the zx-plane (top left), yx-plane (bottom left), and zy-plane (middle) for a single frequency $k = 0.973k_0$ for a square reflector $[9, 11]\lambda_0 \times [4, 6]\lambda_0$ placed at $z = 19\lambda_0$. In the right plot we show the three-dimensional reconstruction of the square reflector.*

length corresponding to the central frequency, while the SNR depends on the bandwidth. We observe a net improvement in the reconstructions compared to the infinite waveguide case and recover the reflector's location, size, and shape with very good accuracy. This is intuitively expected since in the terminating waveguide we benefit from the reflections (multiple-scattering paths) that bounce off the terminating boundary of the waveguide providing views of the reflector that are not available in the infinite waveguide. Our numerical results illustrate the robustness of the method for different array apertures ranging from full to one-fourth of the waveguide's depth. We also obtain good reconstructions for synthetic array data obtained with a single transmit/receive element. Although the methodology was presented here in the two-dimensional case, the extension of the methodology to a three-dimensional waveguide with bounded cross-section does not present any conceptual difficulties.

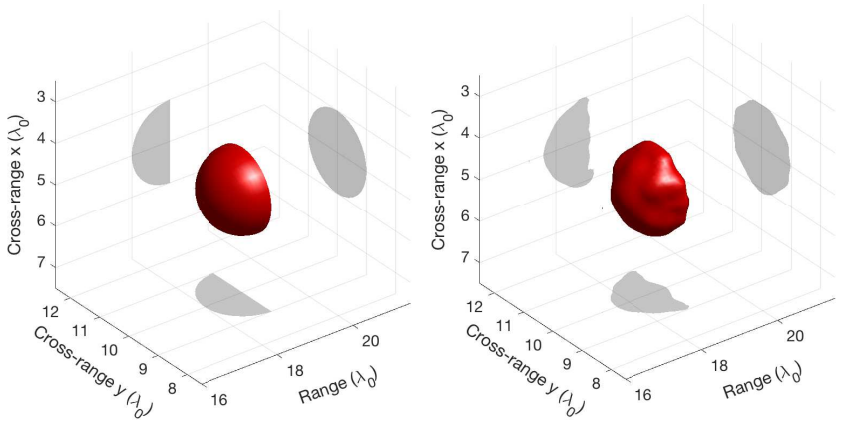

Figure 23. *Imaging a hemisphere with diameter $b = 2\lambda_0$, centered at $\vec{\boldsymbol{x}}^* = (19, 5, 10)\lambda_0$. The true reflector is shown on the left. The modulus of $\mathcal{I}^{\text{a}}$ for a single frequency $k_c = 0.9733k_0$ is shown in the right plot.*

Appendix A. The Kirchhoff–Helmholtz identity in a terminating waveguide. Let $\Omega = \Omega_{L^-} \cup \Omega_{L^+}$ be the terminating waveguide described in section 2; see Figure 1. We assume that all the inhomogeneities of the medium are contained in Ω_{L^+} and that the wave speed is constant in Ω_{L^-}. Let also $\{\mu_n, X_n\}_{n=1}^{\infty}$ be the eigenvalues and eigenvectors of the negative Dirichlet Laplacian $-d^2/dx^2$ in $(0, D)$ given in (30). We will consistently assume that the constant wavenumber, denoted by k, satisfies in Ω_{L^-}

$$\mu_M < k^2 < \mu_{M+1} \quad \text{for some index } M,$$

and we let β_n denote the horizontal wavenumbers in Ω_{L^-} that are given in (6). Hence M is the number of *propagating modes* in Ω_{L^-}.

For any $z_a < L$, let $\mathcal{A} = \{(z_a, x) : \ 0 \le x \le D\}$ be the corresponding cross-section to the range direction, and let $\Omega_{\mathcal{A}}$ denote the bounded domain $\Omega \cap \{(z, x) \in \mathbb{R}^2 : \ z \ge z_a\}$. Note that here we are using the symbol $\mathcal{A}$ to denote an artificial boundary, whereas in previous sections it denoted the array. Then, the eigenpairs $\{\mu_n, X_n\}_n$ allow us to define a *Dirichlet-to-Neumann (DtN)* map (see, e.g., [15]), denoted by T, such that for each function u in suitable function space,

$$Tu(z, x) := \sum_{n=1}^{\infty} i\beta_n u_n(z) X_n(x) = T_1 u(z, x) + T_2 u(z, x), \tag{48}$$

where

$$T_1 u(z, x) = i \sum_{n=1}^{M} \sqrt{k^2 - \mu_n}\, u_n(z) X_n(x), \tag{49}$$

$$T_2 u(z, x) = - \sum_{n=M+1}^{\infty} \sqrt{\mu_n - k^2}\, u_n(z) X_n(x), \tag{50}$$

and

$$u_n(z) := \int_0^D u(z,x)\, X_n(x)\, dx \tag{51}$$

are the Fourier coefficients of u with respect to the orthonormal basis $\{X_n\}_{n=1,2,\dots}$.

Remark A.1.

1. On the artificial boundary $\mathcal{A}$ we may define the following norms of fractional order:

$$\|u\|_{X^s(\mathcal{A})} := \left(\sum_{n=1}^{\infty} (\mu_n)^s |u_n(z_a)|^2\right)^{1/2} < \infty.$$

   The spaces $X^s(\mathcal{A})$, $s \geq 0$, are then defined as the domain of $(-d^2/dy^2)^{s/2}$, while the space of negative order $X^{-s}(\mathcal{A})$ may be identified with the dual of $X^s(\mathcal{A})$. The notation is adopted from [2].
   The function space $X^s(\mathcal{A})$ coincides with $H^s(\mathcal{A})$ for $0 < s < 1/2$. For $s = 1/2$, $X^{1/2}(\mathcal{A})$ may be identified with $H_{00}^{1/2}(\mathcal{A})$, the subspace of functions of $H^{1/2}(\mathcal{A})$ which, when extended by zero, belong to $H^{1/2}(\partial\Omega_{\mathcal{A}})$. For $1/2 < s \leq 1$, $X^s(\mathcal{A}) = \overset{0}{H}{}^s(\mathcal{A})$ (see [22, 2]). Then T is a bounded linear operator from $X^{1/2}(\mathcal{A})$ to $X^{-1/2}(\mathcal{A})$.
2. It is easy to show the following properties of the DtN operator. First,

$$\int_{\mathcal{A}} Tu\, v = \int_{\mathcal{A}} Tv\, u, \tag{52}$$

   and second, letting

$$\begin{aligned} &T^*u(z,x) = T_1^*u(z,x) + T_2u(z,x), \\ \text{where} \quad &T_1^*u(z,x) = -i\sum_{n=1}^{\infty} \sqrt{k^2-\mu_n}\, u_n(z) X_n(x), \end{aligned} \tag{53}$$

   it holds that

$$\overline{Tu} = T^*\overline{u}. \tag{54}$$

Now let $\widehat{G}(\cdot, \vec{\boldsymbol{x}}_i)$ denote the Green's function for the Helmholtz operator with Dirichlet conditions on the boundary $\partial\Omega$ due to a point source located at $\vec{\boldsymbol{x}}_i = (z_i, x_i) \in \Omega_{L_+}$ for a fixed single frequency. (Here we consider a single frequency, so when we refer to the Green's function we omit writing dependence on frequency.) Thus $\widehat{G}(\cdot, \vec{\boldsymbol{x}}_i)$ solves the problem

$$-\Delta\widehat{G}(\cdot, \vec{\boldsymbol{x}}_i) - k^2\eta(\cdot)\,\widehat{G}(\cdot, \vec{\boldsymbol{x}}_i) = \delta(\cdot - \vec{\boldsymbol{x}}_i) \text{ in } \Omega_{\mathcal{A}}, \tag{55}$$

$$\widehat{G}(\cdot, \vec{\boldsymbol{x}}_i) = 0 \text{ on } \partial\Omega_{\mathcal{A}} \setminus \mathcal{A}, \tag{56}$$

$$\partial_\nu\widehat{G}(\cdot, \vec{\boldsymbol{x}}_i) = T\widehat{G}(\cdot, \vec{\boldsymbol{x}}_i) \text{ on } \mathcal{A}, \tag{57}$$

where ν is the outward unit normal on $\mathcal{A}$, and where the last boundary condition, which is imposed on the artificial boundary $\mathcal{A}$, accounts for the radiation condition.

In the following proposition we prove a reciprocity relation for the Green's function.

Proposition A.2. *For any $\vec{\boldsymbol{x}}_1, \vec{\boldsymbol{x}}_2 \in \Omega_{\mathcal{A}}$ it holds that*

$$\widehat{G}(\vec{\boldsymbol{x}}_1, \vec{\boldsymbol{x}}_2) = \widehat{G}(\vec{\boldsymbol{x}}_2, \vec{\boldsymbol{x}}_1). \tag{58}$$

Proof. Let $\vec{\boldsymbol{x}}_i \in \Omega_{\mathcal{A}}$, $i = 1, 2$. Since $\widehat{G}(\cdot, \vec{\boldsymbol{x}}_i)$ satisfies (55), we have for every $\vec{\boldsymbol{y}} = (z, x) \in \Omega_{\mathcal{A}}$ that

$$\begin{aligned} \Delta\widehat{G}(\vec{\boldsymbol{y}}, \vec{\boldsymbol{x}}_2) + k^2\eta(\vec{\boldsymbol{y}})\,\widehat{G}(\vec{\boldsymbol{y}}, \vec{\boldsymbol{x}}_2) &= -\delta(\vec{\boldsymbol{y}} - \vec{\boldsymbol{x}}_2), \\ \Delta\widehat{G}(\vec{\boldsymbol{y}}, \vec{\boldsymbol{x}}_1) + k^2\eta(\vec{\boldsymbol{y}})\,\widehat{G}(\vec{\boldsymbol{y}}, \vec{\boldsymbol{x}}_1) &= -\delta(\vec{\boldsymbol{y}} - \vec{\boldsymbol{x}}_1). \end{aligned}$$

We multiply the first equation by $\widehat{G}(\vec{\boldsymbol{y}}, \vec{\boldsymbol{x}}_1)$, the second by $\widehat{G}(\vec{\boldsymbol{y}}, \vec{\boldsymbol{x}}_2)$, and subtract and integrate the resulting equation over $\Omega_{\mathcal{A}}$ to obtain that

$$\int_{\Omega_{\mathcal{A}}} \Big(\Delta\widehat{G}(\vec{\boldsymbol{y}}, \vec{\boldsymbol{x}}_2)\,\widehat{G}(\vec{\boldsymbol{y}}, \vec{\boldsymbol{x}}_1) - \widehat{G}(\vec{\boldsymbol{y}}, \vec{\boldsymbol{x}}_2)\,\Delta\widehat{G}(\vec{\boldsymbol{y}}, \vec{\boldsymbol{x}}_1) \Big) = \widehat{G}(\vec{\boldsymbol{x}}_1, \vec{\boldsymbol{x}}_2) - \widehat{G}(\vec{\boldsymbol{x}}_2, \vec{\boldsymbol{x}}_1).$$

Using the second Green's identity and the Dirichlet boundary conditions (56), the equation above may be written as

$$\begin{aligned} \widehat{G}(\vec{\boldsymbol{x}}_1, \vec{\boldsymbol{x}}_2) - \widehat{G}(\vec{\boldsymbol{x}}_2, \vec{\boldsymbol{x}}_1) &= \int_{\mathcal{A}} \Big(\frac{\partial\widehat{G}}{\partial\nu}(\vec{\boldsymbol{y}}, \vec{\boldsymbol{x}}_2)\widehat{G}(\vec{\boldsymbol{y}}, \vec{\boldsymbol{x}}_1) - \widehat{G}(\vec{\boldsymbol{y}}, \vec{\boldsymbol{x}}_2)\frac{\partial\widehat{G}}{\partial\nu}(\vec{\boldsymbol{y}}, \vec{\boldsymbol{x}}_1) \Big) \\ &\overset{(57)}{=} \int_{\mathcal{A}} \Big(T\widehat{G}((z_a, x), \vec{\boldsymbol{x}}_2)\,\widehat{G}((z_a, x), \vec{\boldsymbol{x}}_1) - \widehat{G}((z_a, x), \vec{\boldsymbol{x}}_2)\,T\widehat{G}((z_a, x), \vec{\boldsymbol{x}}_1) \Big)\, dx \overset{(52)}{=} 0. \end{aligned}$$

Hence $\widehat{G}(\vec{\boldsymbol{x}}_1, \vec{\boldsymbol{x}}_2) - \widehat{G}(\vec{\boldsymbol{x}}_2, \vec{\boldsymbol{x}}_1) = 0$. ∎

Now we are in a position to prove the following Kirchhoff–Helmholtz identity.

Proposition A.3 (Kirchhoff–Helmholtz identity). *Let $\vec{\boldsymbol{x}}_1, \vec{\boldsymbol{x}}_2 \in \Omega_{\mathcal{A}}$. Then*

$$\widehat{G}(\vec{\boldsymbol{x}}_1, \vec{\boldsymbol{x}}_2) - \overline{\widehat{G}(\vec{\boldsymbol{x}}_1, \vec{\boldsymbol{x}}_2)} = \int_{\mathcal{A}} \Big(\overline{\widehat{G}(\vec{\boldsymbol{y}}, \vec{\boldsymbol{x}}_1)}\nabla\widehat{G}(\vec{\boldsymbol{y}}, \vec{\boldsymbol{x}}_2) - \widehat{G}(\vec{\boldsymbol{y}}, \vec{\boldsymbol{x}}_2)\overline{\nabla\widehat{G}(\vec{\boldsymbol{y}}, \vec{\boldsymbol{x}}_1)} \Big) \cdot \nu\, dx. \tag{59}$$

Moreover,

$$\widehat{G}(\vec{\boldsymbol{x}}_1, \vec{\boldsymbol{x}}_2) - \overline{\widehat{G}(\vec{\boldsymbol{x}}_1, \vec{\boldsymbol{x}}_2)} = 2i \sum_{n=1}^{M} \beta_n\, \overline{\widehat{G}_n(z_a, \vec{\boldsymbol{x}}_1)}\, \widehat{G}_n(z_a, \vec{\boldsymbol{x}}_2), \tag{60}$$

where the Fourier coefficients $\widehat{G}_n(z_a, \cdot)$ are defined in (12).

Proof. Since $\widehat{G}(\cdot, \vec{\boldsymbol{x}}_1)$ solves (55)–(57), it is immediate to show that $\overline{\widehat{G}(\cdot, \vec{\boldsymbol{x}}_1)}$ solves the problem

$$-\Delta\overline{\widehat{G}(\cdot, \vec{\boldsymbol{x}}_1)} - k^2\eta(\cdot)\,\overline{\widehat{G}(\cdot, \vec{\boldsymbol{x}}_1)} = \delta(\cdot - \vec{\boldsymbol{x}}_1) \text{ in } \Omega_{\mathcal{A}}, \tag{61}$$

$$\overline{\widehat{G}(\cdot, \vec{\boldsymbol{x}}_1)} = 0 \text{ on } \partial\Omega_{\mathcal{A}} \setminus \mathcal{A}, \tag{62}$$

$$\partial_\nu\overline{\widehat{G}(\cdot, \vec{\boldsymbol{x}}_1)} = T^*\overline{\widehat{G}(\cdot, \vec{\boldsymbol{x}}_1)} \text{ on } \mathcal{A}. \tag{63}$$

Hence, for every $\vec{\boldsymbol{y}} = (z, x) \in \Omega_{\mathcal{A}}$ we have that

$$\Delta \widehat{G}(\vec{\boldsymbol{y}}, \vec{\boldsymbol{x}}_2) + k^2 \eta(\vec{\boldsymbol{y}})\, \widehat{G}(\vec{\boldsymbol{y}}, \vec{\boldsymbol{x}}_2) = -\delta(\vec{\boldsymbol{y}} - \vec{\boldsymbol{x}}_2),$$
$$\Delta \overline{\widehat{G}(\vec{\boldsymbol{y}}, \vec{\boldsymbol{x}}_1)} + k^2 \eta(\vec{\boldsymbol{y}})\, \overline{\widehat{G}(\vec{\boldsymbol{y}}, \vec{\boldsymbol{x}}_1)} = -\delta(\vec{\boldsymbol{y}} - \vec{\boldsymbol{x}}_1).$$

Now, we multiply the first by $\overline{\widehat{G}(\vec{\boldsymbol{y}}, \vec{\boldsymbol{x}}_1)}$, the second by $\widehat{G}(\vec{\boldsymbol{y}}, \vec{\boldsymbol{x}}_2)$, subtract, integrate over $\Omega_{\mathcal{A}}$, and use the reciprocity property (58) to obtain that

$$\int_{\Omega_{\mathcal{A}}} \left(\Delta \widehat{G}(\vec{\boldsymbol{y}}, \vec{\boldsymbol{x}}_2) \overline{\widehat{G}(\vec{\boldsymbol{y}}, \vec{\boldsymbol{x}}_1)} - \widehat{G}(\vec{\boldsymbol{y}}, \vec{\boldsymbol{x}}_2) \Delta \overline{\widehat{G}(\vec{\boldsymbol{y}}, \vec{\boldsymbol{x}}_1)} \right) = \widehat{G}(\vec{\boldsymbol{x}}_1, \vec{\boldsymbol{x}}_2) - \overline{\widehat{G}(\vec{\boldsymbol{x}}_1, \vec{\boldsymbol{x}}_2)}.$$

Now, (59) results using the second Green's identity and the boundary conditions (56) and (62).

Moreover, from (59) and the DtN conditions (57) and (63) we deduce that

$$\begin{aligned} &\widehat{G}(\vec{\boldsymbol{x}}_1, \vec{\boldsymbol{x}}_2) - \overline{\widehat{G}(\vec{\boldsymbol{x}}_1, \vec{\boldsymbol{x}}_2)} \\ &= \int_{\mathcal{A}} \left(\overline{\widehat{G}((z_a, x), \vec{\boldsymbol{x}}_1)} T \widehat{G}((z_a, x), \vec{\boldsymbol{x}}_2) - \widehat{G}((z_a, x), \vec{\boldsymbol{x}}_2) T^* \overline{\widehat{G}((z_a, x), \vec{\boldsymbol{x}}_1)} \right) dx \\ &\overset{(52)}{=} \int_{\mathcal{A}} \left(T \overline{\widehat{G}((z_a, x), \vec{\boldsymbol{x}}_1)} - T^* \overline{\widehat{G}((z_a, x), \vec{\boldsymbol{x}}_1)} \right) \widehat{G}((z_a, x), \vec{\boldsymbol{x}}_2)\, dx. \end{aligned} \tag{64}$$

Therefore, in view of (49) and (53), we get that

$$T \overline{\widehat{G}((z_a, x), \vec{\boldsymbol{x}}_1)} - T^* \overline{\widehat{G}((z_a, x), \vec{\boldsymbol{x}}_1)} = 2i \sum_{n=1}^{M} \beta_n\, \overline{\widehat{G}_n(z_a, \vec{\boldsymbol{x}}_1)}\, X_n(x).$$

Inserting the above in (64) we conclude that

$$\begin{aligned} \widehat{G}(\vec{\boldsymbol{x}}_1, \vec{\boldsymbol{x}}_2) - \overline{\widehat{G}(\vec{\boldsymbol{x}}_1, \vec{\boldsymbol{x}}_2)} &= 2i \int_0^D \sum_{n=1}^{M} \beta_n\, \overline{\widehat{G}_n(z_a, \vec{\boldsymbol{x}}_1)}\, X_n(x)\, \widehat{G}(z_a, x, \vec{\boldsymbol{x}}_2)\, dx \\ &= 2i \sum_{n=1}^{M} \beta_n\, \overline{\widehat{G}_n(z_a, \vec{\boldsymbol{x}}_1)} \int_0^D \widehat{G}(z_a, x, \vec{\boldsymbol{x}}_2)\, X_n(x)\, dx, \end{aligned}$$

which completes the proof. ∎

Appendix B. Derivation of $\widehat{G}^R$. In this section we present the derivation of the Green's function $\widehat{G}^R$ for the Helmholtz operator when the terminating waveguide Ω is a homogeneous ($\eta(\vec{\boldsymbol{x}}) = 1$) semi-infinite strip. Specifically, $\Omega = (-\infty, R) \times (0, D)$. Then the Green's function $\widehat{G}^R(\cdot, \vec{\boldsymbol{x}}_s; \omega)$ due to a point source located at $\vec{\boldsymbol{x}}_s = (z_s, x_s) \in \Omega$, for a single frequency ω, solves the problem

$$\begin{aligned} -\Delta \widehat{G}(\cdot, \vec{\boldsymbol{x}}_s; \omega) - k^2 \widehat{G}(\cdot, \vec{\boldsymbol{x}}_s; \omega) = \delta(\cdot - \vec{\boldsymbol{x}}_s) \quad &\text{in } \Omega, \\ \widehat{G}(\cdot, \vec{\boldsymbol{x}}_s; \omega) = 0 \text{ on } \partial\Omega. \end{aligned}$$

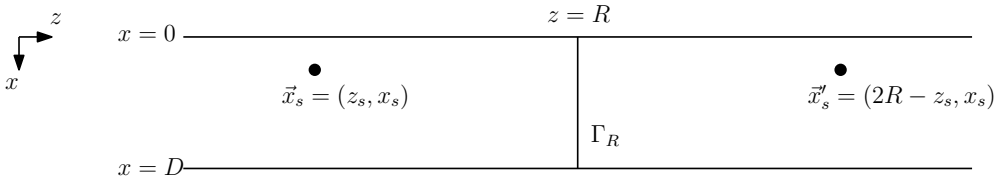

Figure 24. *Two sources placed symmetrically with respect to* Γ_R.

In order to derive an analytic expression for $\widehat{G}^R(\cdot, \vec{\boldsymbol{x}}_s; \omega)$ we will use the method of images [10]. With reference to Figure 24, we assume an infinite waveguide in the z-direction and add a source at $\vec{\boldsymbol{x}}'_s$ that is symmetric to $\vec{\boldsymbol{x}}_s$ with respect to Γ_R, i.e., $\vec{\boldsymbol{x}}'_s = (2R - z_s, x_s)$.

We then compute the field at a point $\vec{\boldsymbol{y}} = (z, x) \in \Omega$ as

$$\widehat{G}^R(\vec{\boldsymbol{y}}, \vec{\boldsymbol{x}}_s; \omega) = \widehat{G}^0(\vec{\boldsymbol{y}}, \vec{\boldsymbol{x}}_s; \omega) - \widehat{G}^0(\vec{\boldsymbol{y}}, \vec{\boldsymbol{x}}'_s; \omega), \tag{65}$$

where $\widehat{G}^0(\vec{\boldsymbol{y}}, \vec{\boldsymbol{x}}_s; \omega)$ denotes the Green's function for an infinite waveguide. A normal mode representation of $\widehat{G}^0(\cdot, \vec{\boldsymbol{x}}_s; \omega)$ reads [19, 27]

$$\widehat{G}^0(\vec{\boldsymbol{x}}, \vec{\boldsymbol{x}}_s; \omega) = \frac{i}{2} \sum_{m=1}^{\infty} \frac{\mathrm{e}^{i\beta_m |z - z_s|}}{\beta_m} X_m(x) X_m(x_s),$$

where $\{\mu_n, X_n\}_{n=1}^{\infty}$ are the eigenvalues and eigenvectors of $-d^2/dx^2$ in $(0, D)$ given in (30), and β_n are the horizontal wavenumbers; see (6).

Then, (65) implies that

$$\begin{aligned}
\widehat{G}^R(\vec{\boldsymbol{y}}, \vec{\boldsymbol{x}}_s) &= \frac{i}{2} \sum_{m=1}^{\infty} \frac{\mathrm{e}^{i\beta_m |z - z_s|}}{\beta_m} X_m(x) X_m(x_s) - \frac{i}{2} \sum_{n=1}^{\infty} \frac{\mathrm{e}^{i\beta_n |z - 2R + z_s|}}{\beta_n} X_n(x) X_n(x_s) \\
&= \frac{i}{2} \sum_{m=1}^{\infty} \frac{\mathrm{e}^{i\beta_m |z - z_s|} - \mathrm{e}^{i\beta_m |z + z_s - 2R|}}{\beta_m} X_m(x) X_m(x_s),
\end{aligned}$$

where $z < R$ and $0 \le x \le D$. Since $z, z_s < R$, it turns out that $z + z_s - 2R < 0$, and hence

$$\begin{aligned}
\widehat{G}^R(\vec{\boldsymbol{y}}, \vec{\boldsymbol{x}}_s) &= \frac{i}{2} \sum_{m=1}^{\infty} \frac{\mathrm{e}^{i\beta_m |z - z_s|} - \mathrm{e}^{-i\beta_m (z + z_s - 2R)}}{\beta_m} X_m(x) X_m(x_s) \\
&= \begin{cases}
\displaystyle\sum_{m=1}^{\infty} \frac{i}{2\beta_m} \left(\mathrm{e}^{i\beta_m (z - z_s)} - \mathrm{e}^{-i\beta_m (z + z_s - 2R)} \right) X_m(x) X_m(x_s), & z > z_s, \\
\displaystyle\sum_{m=1}^{\infty} \frac{i}{2\beta_m} \left(\mathrm{e}^{-i\beta_m (z - z_s)} - \mathrm{e}^{-i\beta_m (z + z_s - 2R)} \right) X_m(x) X_m(x_s), & z < z_s.
\end{cases}
\end{aligned} \tag{66}$$

Notice that

$$\begin{aligned}
\mathrm{e}^{i\beta_m (z - z_s)} - \mathrm{e}^{-i\beta_m (z + z_s - 2R)} &= \mathrm{e}^{i\beta_m (R - z_s)} \left(\mathrm{e}^{i\beta_m (z - R)} - \mathrm{e}^{-i\beta_m (z - R)} \right) \\
&= -2i \, \mathrm{e}^{i\beta_m (R - z_s)} \, \sin \beta_m (R - z)
\end{aligned}$$

and, similarly,

$$\mathrm{e}^{-i\beta_m(z-z_s)} - \mathrm{e}^{-i\beta_m(z+z_s-2R)} = -2i\,\mathrm{e}^{i\beta_m(R-z)}\,\sin\beta_m(R-z_s).$$

Therefore, (66) may also be written as

$$\widehat{G}^R(\vec{\boldsymbol{y}},\vec{\boldsymbol{x}}_s) = \begin{cases} \displaystyle\sum_{m=1}^{\infty} \frac{1}{\beta_m}\,\mathrm{e}^{i\beta_m(R-z_s)}\,\sin\beta_m(R-z)\,X_m(x)\,X_m(x_s), & z > z_s, \\ \displaystyle\sum_{m=1}^{\infty} \frac{1}{\beta_m}\,\mathrm{e}^{i\beta_m(R-z)}\,\sin\beta_m(R-z_s)\,X_m(x)\,X_m(x_s), & z < z_s. \end{cases} \tag{67}$$

Acknowledgment. The inspiring ICERM/Brown University research environment and its kind hospitality are warmly acknowledged.

REFERENCES

[1] M. Abramowitz and I. A. Stegun, *Handbook of Mathematical Functions with Formulas, Graphs, and Mathematical Tables*, Dover, 1964.
[2] A. Bendali and P. Guillaume, *Non-reflecting boundary conditions for waveguides*, Math. Comput., 68 (1999), pp. 123–144.
[3] L. Borcea, J. Garnier, and C. Tsogka, *A quantitative study of source imaging in random waveguides*, Commun. Math. Sci., 13 (2015), pp. 749–776.
[4] L. Borcea and D.-L. Nguyen, *Imaging with electromagnetic waves in terminating waveguides*, Inverse Probl. Imaging, 10 (2016), pp. 915–941.
[5] L. Borcea, G. Papanicolaou, and F. Guevara Vasquez, *Edge illumination and imaging of extended reflectors*, SIAM J. Imaging Sci., 1 (2008), pp. 75–114, https://doi.org/10.1137/07069290X.
[6] L. Bourgeois, F. Le Louër, and E. Lunéville, *On the use of Lamb modes in the linear sampling method for elastic waveguides*, Inverse Problems, 27 (2011), 055001.
[7] L. Bourgeois and E. Lunéville, *The linear sampling method in a waveguide: A modal formulation*, Inverse Problems, 24 (2008), 015018.
[8] L. Bourgeois and E. Lunéville, *On the use of sampling methods to identify cracks in acoustic waveguides*, Inverse Problems, 28 (2012), 105011.
[9] J. L. Buchanan, R. P. Gilbert, A. Wirgin, and Y. S. Xu, *Marine Acoustics: Direct and Inverse Problems*, SIAM, 2004, https://doi.org/10.1137/1.9780898717983.
[10] D. Cheng, *Field and Wave Electromagnetics*, Addison-Wesley Ser. Elec. Engrg., Addison-Wesley Publishing Company, 1989.
[11] D. Colton and H. Haddar, *An application of the reciprocity gap functional to inverse scattering theory*, Inverse Problems, 21 (2005), pp. 383–398.
[12] D. Colton and A. Kirsch, *A simple method for solving inverse scattering problems in the resonance region*, Inverse Problems, 12 (1996), pp. 383–393.
[13] S. Dediu and J. R. McLaughlin, *Recovering inhomogeneities in a waveguide using eigensystem decomposition*, Inverse Problems, 22 (2006), pp. 1227–1246.
[14] D. Evans and R. Porter, *Trapped modes embedded in the continuous spectrum*, Quart. J. Mech. Appl. Math., 51 (1998), pp. 263–274.
[15] C. I. Goldstein, *A finite element method for solving Helmholtz type equations in waveguides and other unbounded domains*, Math. Comp., 39 (1982), pp. 309–324.
[16] I. S. Gradshteyn and I. M. Ryzhik, *Table of Integrals, Series, and Products*, 7th ed., Elsevier/Academic Press, 2007.

[17] M. Ikehata, G. N. Makrakis, and G. Nakamura, *Inverse boundary value problem for ocean acoustics using point sources*, Math. Methods Appl. Sci., 27 (2004), pp. 1367–1384.
[18] D. R. Jackson and D. R. Dowling, *Phase conjugation in underwater acoustics*, J. Acoust. Soc. Amer., 89 (1991), pp. 171–181.
[19] F. Jensen, W. Kuperman, M. Porter, and H. Schmidt, *Computational Ocean Acoustics*, Modern Acoust. Signal Process., Springer, 2011.
[20] D. S. Jones, *The eigenvalues of* $\nabla^2 u + \lambda u = 0$ *when the boundary conditions are given on semi-infinite domains*, Proc. Cambridge Philos. Soc., 49 (1953), pp. 668–684.
[21] A. Kirsch, *Characterization of the shape of a scattering obstacle using the spectral data of the far field operator*, Inverse Problems, 14 (1998), pp. 1489–1512.
[22] J.-L. Lions and E. Magenes, *Non-homogeneous Boundary Value Problems and Applications. Vol.* III, translated from the French by P. Kenneth, Grundlehren Math. Wiss. 183, Springer-Verlag, 1973.
[23] P. Monk and V. Selgas, *Sampling type methods for an inverse waveguide problem*, Inverse Probl. Imaging, 6 (2012), pp. 709–747.
[24] *Montjoie User's Guide*, http://montjoie.gforge.inria.fr/.
[25] N. Mordant, C. Prada, and M. Fink, *Highly resolved detection in a waveguide using the D.O.R.T. method*, J. Acoust. Soc. Amer., 105 (1999), pp. 2634–2642.
[26] F. W. J. Olver, A. B. Olde Daalhuis, D. W. Lozier, B. I. Schneider, R. F. Boisvert, C. W. Clark, B. R. Miller and B. V. Saunders, eds., *NIST Digital Library of Mathematical Functions*, http://dlmf.nist.gov/, Release 1.0.18 of 2018-03-27.
[27] B. Pinçon and K. Ramdani, *Selective focusing on small scatterers in acoustic waveguides using time reversal mirrors*, Inverse Problems, 23 (2007), pp. 1–25.
[28] F. Podd, M. Ali, K. Horoshenkov, A. Wood, S. Tait, J. Boot, R. Long, and A. Saul, *Rapid sonic characterisation of sewer change and obstructions*, Water Sci. Technol., 56 (2007), pp. 131–139.
[29] C. Prada, J. de Rosny, D. Clorennec, J.-G. Minonzio, A. Aubry, M. Fink, L. Berniere, P. Billand, S. Hibral, and T. Folegot, *Experimental detection and focusing in shallow water by decomposition of the time reversal operator*, J. Acoust. Soc. Amer., 122 (2007), pp. 761–768.
[30] C. Tsogka, D. A. Mitsoudis, and S. Papadimitropoulos, *Selective imaging of extended reflectors in two-dimensional waveguides*, SIAM J. Imaging Sci., 6 (2013), pp. 2714–2739, https://doi.org/10.1137/130924238.
[31] C. Tsogka, D. A. Mitsoudis, and S. Papadimitropoulos, *Partial-aperture array imaging in acoustic waveguides*, Inverse Problems, 32 (2016), 125011.
[32] Y. Xu, C. Mawata, and W. Lin, *Generalized dual space indicator method for underwater imaging*, Inverse Problems, 16 (2000), pp. 1761–1776.